

Electronic Thesis and Dissertation Repository

8-14-2020 12:00 PM

TSPO PET Detects Acute Neuroinflammation but not Diffuse Chronically Activated MHCII Microglia in the Rat

Nassir Al-Khishman, *The University of Western Ontario*

Supervisor: Thiessen, Jonathan D., *The University of Western Ontario*

Joint Supervisor: Whitehead, Shawn N., *The University of Western Ontario*

A thesis submitted in partial fulfillment of the requirements for the Master of Science degree in Medical Biophysics

© Nassir Al-Khishman 2020

Follow this and additional works at: <https://ir.lib.uwo.ca/etd>



Part of the [Medical Biophysics Commons](#)

Recommended Citation

Al-Khishman, Nassir, "TSPO PET Detects Acute Neuroinflammation but not Diffuse Chronically Activated MHCII Microglia in the Rat" (2020). *Electronic Thesis and Dissertation Repository*. 7260.
<https://ir.lib.uwo.ca/etd/7260>

This Dissertation/Thesis is brought to you for free and open access by Scholarship@Western. It has been accepted for inclusion in Electronic Thesis and Dissertation Repository by an authorized administrator of Scholarship@Western. For more information, please contact wlsadmin@uwo.ca.

Abstract

Background

Accurate and sensitive imaging biomarkers are required to study the progression of white matter (WM) microglial activation in neurodegenerative diseases *in vivo*. The translocator protein (TSPO) is considered a sensitive target for imaging microglial activation with positron emission tomography (PET). This study aimed to test the ability of TSPO to detect WM microglial activation marked by major histocompatibility complex class II (MHCII) molecules in rat models of prodromal Alzheimer's disease and acute subcortical stroke.

Methods

Fischer 344 wild-type (n = 12) and TgAPP21 (n = 11) rats were imaged with [¹⁸F]FEPPA PET and MRI to investigate TSPO tracer uptake in the corpus callosum. Wild-type rats subsequently received an endothelin-1 (ET1)-induced subcortical stroke and were imaged at days 7 and 28 post-stroke before immunohistochemistry of TSPO, GFAP for astrocytes, iNOS for microglia releasing toxic nitrous oxide, and the MHCII rat antigen, OX6.

Results

[¹⁸F]FEPPA-PET findings that TSPO expression was not increased in WM of TgAPP21 rats and was only increased in the infarct and proximal WM were confirmed by immunohistochemistry (infarct TSPO cells/mm²: day 7 = 555 ± 181; day 28 = 307 ± 153; proximal WMTSPO cells/mm²: day 7 = 113 ± 93; day 28 = 5 ± 7). TSPO and iNOS were not able to detect the chronic WM microglial activation that was detected with MHCII in the contralateral corpus callosum (day 28 OX6 % area: saline = 0.62 ± 0.38; stroke = 4.30 ± 2.83; *P* = .029).

Conclusion

Within the regions and groups investigated, TSPO was only expressed in the stroke-induced insult and proximal tissue, and therefore was unable to detect remote and non-insult-related chronically activated microglia overexpressing MHCII in WM.

Keywords

TSPO; major histocompatibility complex class II; white matter inflammation; ischemic stroke; Alzheimer's disease

Lay summary

Background

Accurate and sensitive biomarkers are required to study the progression of inflammation in neurological diseases. To image white matter inflammation in living subjects, researchers can produce radioactive molecules that bind to proteins in the body that serve as markers of inflammation, inject them into the subject, then image them with positron emission tomography (PET). Our group set out to investigate whether a protein known as the translocator protein can be detected, in living subjects, in a type of white matter inflammation that we previously associated with Alzheimer's disease and deep stroke and can currently only be imaged after death. We hypothesized that the translocator protein expression can be detected in rats with Alzheimer's Disease at the white matter and in rats with deep stroke at white matter that was distant from the stroke.

Methods

Rats that were non-genetically modified (n = 12) and genetically modified to express a protein associated with Alzheimer's Disease (n = 11) were injected with the radioactive molecule [¹⁸F]FEPPA to image the translocator protein using PET. After initial assessment of white matter inflammation, the non-genetically modified rats received a deep stroke and were imaged again at days 7 and 28 post-stroke. The rats were sacrificed to investigate their expression of the translocator protein, other inflammatory proteins, and a protein that indicates our target inflammation, OX6.

Results

[¹⁸F]FEPPA positron emission tomography only detected inflammation in the stroke region of rats that received the deep stroke; the distant white matter inflammation we wanted to image was not detected. Inflammation was detected in distant white matter using post-mortem microscopy of the inflammatory molecule OX6, but it was not detectable using the translocator protein, irrespective of the binding molecule used.

Conclusion

Within the regions and groups investigated, the translocator protein was only able to detect inflammation near the stroke region, and therefore was not able to detect the distant and non-injury-related yet pathologically important white matter inflammation that we wanted to detect. To detect that white matter inflammation with PET, new radioactive molecules will need to be developed.

Co-authorship statement

Chapter 1 and 3 were written by Nassir U. Al-Khishman and edited by the Principal Investigators Dr. Shawn N. Whitehead and Dr. Jonathan D. Thiessen.

In chapter 2, an integrated article was submitted to EJNNMI Research with the following co-authorship statement: Nassir U. Al-Khishman analyzed, interpreted, and helped collect the majority of the data and was a major contributor in writing the manuscript. Qi Qi helped collect the majority of the PET data, developed the design and analysis of radiometabolite analysis, and contributed to the manuscript. Austyn D. Roseborough helped collect the majority of the PET data, coordinated volunteers to help with the collection of immunohistochemistry data, helped interpret the results, and contributed to the manuscript. Dr. Alexander Levit helped develop the PET data collection methods, helped interpret the results, and contributed to the manuscript. Dr. Brian L. Allman helped develop the research question, helped interpret the results, and contributed to the manuscript. Dr. Udunna C. Anazodo led the development of radiometabolite analysis, helped guide the PET analysis, helped interpret the results, and contributed to the manuscript. Dr. Matthew S. Fox was instrumental in collecting the PET data and contributed to the manuscript. Dr. Shawn N. Whitehead, who was an equal last coauthor, helped develop the research question, led the collection, and analysis of the immunohistochemistry data and was a major contributor to interpretation and writing the manuscript. Dr. Jonathan D. Thiessen helped develop the research question, led the collection, and analysis of the PET data and was a major contributor to interpretation and writing the manuscript. All authors read and approved the final manuscript.

Dedication

This manuscript is dedicated to (i) Canada, who took me and my siblings in and gave me a home with many opportunities, and (ii) the internet, which made it (and continues to make it) trivial for me and others to gain access to the wealth of human knowledge.

Acknowledgements

First, I'd like to thank my two supervisors, Jonathan Thiessen and Shawn Whitehead. The two of you were an amazing combination for me.

Jonathan, I had a feeling that you would be a great supervisor from the day that I met you; I don't remember where we went on that short tour, but I remember thinking "this guy is pretty open-minded". Sure enough, you proved that everyday with your eagerness to understand other fields. Most of all, thank you for being a critical thinker and a great leader. Your patience was admirable, and your optimism was infectious. Thank you for seeing the best in me and others.

Shawn, thank you for being a huge inspiration. Your ability to manage and such a large lab and give us the time we need to work on our research skills and soft skills is impressive. Definitely, you really helped me refine my presentation and differentiation. Thank you for caring. Finally, thanks for the fun times - I don't think I'll ever be able to think of criss-cross fries without thinking about striatal white matter.

I would also like to thank my advisory committee members Brian Allman and Udanna Anazodo. Your support has been touching, and your passion for my research, and your research, definitely comes through when you talk. I learned a lot from both of you. It was a privilege to have you on my committee.

Additionally, I would like to thank everyone else who also had a huge impact, perhaps in ways you did not know, on my journey of research and education thus far: Frank Prato, Savita Dhanvantari, Keith St. Lawrence, Justin Hicks, Ajay Rajaram, Lawrence Yip, and Matthew Teeter.

Lastly, I would to thank my friends and admin in the departments of *Medical Biophysics* and *Anatomy and Cell Biology*, the *Vulnerable Brain Lab*, and the *Hybrid Imaging Lab*. Thank you for all the laughs and support.

Table of Contents

ABSTRACT	II
LAY SUMMARY	IV
CO-AUTHORSHIP STATEMENT	VI
DEDICATION	VII
ACKNOWLEDGEMENTS	VIII
TABLE OF CONTENTS	X
LIST OF FIGURES	XIII
LIST OF APPENDICES	XV
LIST OF ABBREVIATIONS AND SYMBOLS	XVI
SYMBOLS	XVIII
CHAPTER 1: INTRODUCTION	1
1.1 WHITE MATTER (WM) IMPORTANCE AND FUNCTION	1
1.2 INFLAMMATION AND MICROGLIAL ACTIVATION	2
1.2.1 <i>Microglia</i>	3
1.2.2 <i>Astrocytes</i>	3
1.3 SUBCORTICAL STROKE.....	4
1.3.1 <i>Subcortical Stroke Etiology</i>	4
1.3.2 <i>Stroke Molecular Changes</i>	5
1.3.3 <i>Stroke Infarct Core and Penumbra</i>	5
1.3.4 <i>WM Microglial Activation and Disease in Subcortical Stroke</i>	6
1.3.5 <i>WM Disease Relationship with Cognition in Subcortical Stroke</i>	8
1.4 ALZHEIMER’S DISEASE (AD)	9
1.4.1 <i>AD Stages and Diagnosis</i>	9
1.4.2 <i>WM Microglial Activation and Disease in AD</i>	10
1.5 MEASURING WM MICROGLIAL ACTIVATION.....	13
1.5.1 <i>Major Histocompatibility Complex Class II (MHCII) Molecules</i>	13
1.5.2 <i>Translocator Protein (TSPO)</i>	14
1.6 POSITRON EMISSION TOMOGRAPHY (PET)	14
1.6.1 <i>PET Spatial Resolution</i>	16
1.6.2 <i>Radiotracer Target, Sensitivity, and Specificity</i>	16
1.6.3 <i>Tracer Kinetic Modelling</i>	18
1.6.3.1 <i>Compartmental Modelling</i>	19
1.6.3.2 <i>Total Distribution Volume (V_T)</i>	21
1.5.3.3 <i>Logan Graphical Analysis</i>	22
1.6.4 <i>Reference Regions</i>	24
1.6.5 <i>Ex Vivo PET Validation</i>	25
1.6.5.1 <i>Immunohistochemistry (IHC)</i>	25

1.6.6 TSPO-PET.....	26
1.7 RATIONALE AND OBJECTIVES	27
1.8 REFERENCES	29
CHAPTER 2: TSPO PET DETECTS ACUTE NEUROINFLAMMATION BUT NOT DIFFUSE CHRONICALLY ACTIVATED MHCII MICROGLIA IN THE RAT	37
2.1 INTRODUCTION.....	37
2.2 METHODS.....	38
2.2.1 <i>Animals and Experimental Design</i>	38
2.2.2 <i>In Vivo Imaging</i>	39
2.2.2.1 MRI.....	39
2.2.2.2 CT	39
2.2.2.3 PET Acquisition and Processing.....	40
2.2.2.4 PET Analysis	40
2.2.3 <i>Immunohistochemistry</i>	42
2.2.4 <i>Statistical Analysis</i>	43
2.3 RESULTS	44
2.3.1 <i>The Cerebellum is an Appropriate Pseudoreference Region for [¹⁸F]FEPPA PET ...</i>	44
2.3.2 <i>[¹⁸F]FEPPA UR was not Elevated in WM of TgAPP21 Rats.....</i>	46
2.3.3 <i>[¹⁸F]FEPPA UR was not Elevated in Remote WM Following ET1-induced Stroke ...</i>	47
2.3.4 <i>TSPO was not Expressed in Remote WM Following ET1-induced Stroke</i>	48
2.3.5 <i>GFAP and iNOS Expression was not Changed in WM Following ET1-induced Stroke</i>	51
2.3.6 <i>MHCII-Positive Activated Microglia were Chronically Expressed in Remote WM</i> <i>Following ET1-induced Stroke</i>	52
2.4 DISCUSSION	53
2.5 REFERENCES	56
CHAPTER 3: CONCLUSION AND FUTURE DIRECTIONS	61
3.1 SUMMARY	61
3.2 TSPO IN WM	63
3.3 MHCII AS A MARKER OF MICROGLIAL ACTIVATION.....	64
3.4 LIMITATIONS	64
3.4.1 <i>Fischer 344 rat strain may have an overactive inflammatory response</i>	64
3.4.2 <i>Gray Matter in Subcortical Stroke and AD.....</i>	64
3.5 FUTURE DIRECTIONS.....	65
3.5.1 <i>MHCII radiotracers</i>	65
3.5.2 <i>Alzheimer’s Disease and Subcortical Stroke Comorbidity.....</i>	68
3.5.3 <i>Using PET to Guide WM Microglial Activation Therapy</i>	69
3.6 CONCLUSION.....	70
3.7 REFERENCES	71
APPENDICES	74
APPENDIX A: EXAMPLE LOGAN SOLUTION	74

APPENDIX B: TIME-ACTIVITY CURVES	77
APPENDIX C: ANIMAL USE ETHICS APPROVAL.....	78
APPENDIX D: CURRICULUM VITAE	81

List of Figures

Fig 1.1: AD diagnosis	10
Fig 1.2: A visual representation of a 2TCM.....	20
Fig 2.1: Analytical Methods	41
Fig 2.2: SUV was significantly different between the pseudoreference regions, cerebellum and PAG, in wild-type and TgAPP21 [F(1,21)=53.30, P<.0005, two-way ANOVA]	44
Fig 2.3: Wild-type saline and ET1 rat pseudoreference regions at baseline, day 7, and day 28 after an injection in the right dorsal striatum	44
Fig 2.4: Correlations of distribution volume with distribution volume ratio to candidate pseudoreference regions.....	45
Fig 2.5: Correlations of infarct TSPO immunohistochemistry to uptake ratios calculated using candidate pseudoreference regions	45
Fig 2.6: Transgenic amyloid precursor protein rats did not have an elevated [18F]FEPPA PET WM uptake ratio, to the cerebellum, relative to wild-type saline rats	46
Fig 2.7: [18F]FEPPA UR was not elevated in remote WM following ET1-induced stroke	47
Fig 2.8: Immunohistochemistry showed that TSPO, but not iNOS, was elevated in the infarct site of ET1 rats at days 7 and 28 post-stroke	49
Fig 2.9 TSPO Immunohistochemistry of WM at day 7 and day 28 in saline and ET1 rats	50

Fig 2.10: Fig 2.5 WM immunohistochemistry in the contralateral corpus callosum (CC c) showing that at 28 days post-stroke, ET1 rats only showed an elevation of OX6 (MHCII); not TSPO, iNOS, and GFAP51

Fig 3.1. A visual summary of MHC nomenclature65

Fig 3.2. HLA-DR alpha chain alignment between humans and rats.....67

List of Appendices

Appendix A: Example Logan Solution73

Appendix B: Time-activity curves76

Appendix C: Animal Use Ethics Approval.....77

Appendix D: Curriculum Vitae80

List of Abbreviations and Symbols

[¹⁸F]FEPPA: [¹⁸F]-N-(2-(2-fluoroethoxy)benzyl)-n-(4-phenoxy pyridin-3-yl)acetamide

A β : beta-amyloid

AD: Alzheimer's disease

APP: amyloid precursor protein

ANOVA: analysis/analyses of variance

BBB: blood-brain barrier

CC c: contralateral corpus callosum

CC i: ipsilateral corpus callosum

CERAD: consortium to establish a registry for Alzheimer's disease

CIR: contralateral to the infarct region

CNS: central nervous system

CT: computed tomography

DTI: diffusion tensor imaging

DV/V_T: total distribution volume

DVR: DV ratio

ET1: endothelin-1

EJNMII: European Journal of Nuclear Medicine and Molecular Imaging

FA: fractional anisotropy

FLAIR: fluid-attenuated inversion recovery

FOV: field of view

FSE: fast spin echo

GFAP: glial acid fibrillary protein

HLA: human leukocyte antigens

HSD: honestly significant differences

IHC: immunohistochemistry

IR: infarct region

MAP2: microtubule-associated protein 2

MAPT: microtubule-associated protein tau

MTR: magnetization transfer ratio

MHCII: major histocompatibility complex class II

MRI: magnetic resonance imaging

OSEM3D/FMAP: 3D ordered-subset expectation maximization followed by fast maximum a posteriori

PBR: peripheral benzodiazepine receptor

PBS: phosphate-buffered saline

PFA: paraformaldehyde

PET: positron emission tomography

ROI: region of interest

SD: standard deviation

SUV: standardized uptake value

TgAPP21: transgenic Fischer 344 rat that overexpresses human Swedish/Indiana- mutated amyloid precursor protein

TR: repetition time

TSPO: translocator protein

UR: uptake ratio normalized to the cerebellum

WM: white matter

Symbols

BP_{ND} = binding potential; ratio of radiotracer concentration in the specifically bound compartment to that in the nondisplaceable compartment

V_T = total distribution volume

C_T = Concentration of total radioactivity in the tissue

C_p = Concentration of free parent metabolite in the plasma

C_b = Concentration of total radioactivity in whole blood

C_1 = Concentration of parent metabolite in the non-displaceable compartment (2TCM)

C_2 = Concentration of parent metabolite in the bound compartment

V_b = The ROI volume fraction of vascular tissue

K_1 = plasma-to-unbound-compartment transfer rate (delivery)

k_2 = unbound-compartment-to-plasma transfer rate (clearance)

k_3 = unbound-compartment-to-bound-compartment transfer rate (binding)

k_4 = bound-compartment-to-unbound-compartment transfer rate (unbinding)

V_s = distribution volume in the bound compartment

V_{ND} = distribution volume in the nondisplaceable compartment

BP_{ND} = equilibrium ratio of radiotracer concentration in the specifically bound compartment to that in the nondisplaceable compartment

Chapter 1: Introduction

Chronic white matter (WM) inflammation can be observed in subcortical stroke, traumatic brain injury, schizophrenia, and Alzheimer's Disease (AD) [1–4]. In particular, chronic WM microglial activation marked by major histocompatibility complex class II (MHCII) molecules is believed to play an early neurotoxic role [5]. To further our understanding, develop therapeutic approaches, and aid early diagnosis, there is a need to quantify WM MHCII microglial activation in living people. Still, there is no established method for the *in vivo* quantification of WM MHCII microglial activation. In this thesis, the objective was to image chronic WM MHCII microglial activation *in vivo* using translocator protein positron emission tomography (TSPO-PET) in rat models of AD and subcortical stroke. The following introduction presents evidence for why MHCII microglial activation may play a neurotoxic role in AD and subcortical stroke and background for TSPO and PET.

1.1 White Matter (WM) Importance and Function

In vertebrates, brain WM is an important constituent of neuronal networks, which are widely accepted as responsible for motor movement, thoughts, and meaningful behavior [6]. An individual neuron in the networks is composed of a cell body, axons that protrude from the cell body, and dendrites. In the central nervous system (CNS), oligodendrocytes support and wrap axons with multiple layers of myelin. Myelinated axons appear white and therefore form the structure known as WM. By wrapping the entire length of axons except for interspaced nodes with myelin, nerve impulses made up of sodium and potassium ions are forced to occur only at the nodes instead of throughout the entire axon. This is known as saltatory conduction and it makes neuron-neuron communication more rapid by increasing the charge difference along the axonal cytoplasm, which is often called action potential [7]. When myelin is lost, the results include a

reduction in conduction velocity, nerve impulses become less temporally predictable, and nerve impulses often do not lead to downstream activation [7]. As myelin is the main component of white matter, healthy WM is essential for healthy cognitive and motor function.

1.2 Inflammation and Microglial Activation

In general, inflammation can be acute or chronic after an injury, pathogen, or autoimmune response. Acute inflammation occurs in regions that have recently been exposed to an appropriate stimulus, and regions outside the CNS experiencing acute inflammation are influxed with fluid to cause swelling also known as edema. This may cause pain and loss of function by stressing nearby neuroreceptors, and an increased blood flow may cause a red appearance and a feeling of heat [8]. In contrast, chronic inflammation occurs late after a stimulus, and regions outside the CNS experiencing chronic inflammation are usually only associated with changes in signalling molecules, although the molecules are different than those in acute inflammation, and white blood cells such as macrophages [8].

Macrophages and cells with similar lineages, such as microglia in the CNS, are often investigated to study the state of inflammation. The term macrophage is often used to refer to a type of peripheral cell that is able to remove pathogens, dying cells, or debris by releasing reactive oxygen species, phagocytosis, and enzyme-mediated digestion [9]. That said, macrophages also seem to be necessary for the healing processes of re-epithelialization, collagen deposition, and angiogenesis [10].

Inflammation in the CNS, also known as neuroinflammation, is similar to inflammation outside the CNS with respect to the details discussed above. Exceptions include that (i) redness, heat, and pain are not usually reported along with acute neuroinflammation and (ii) a healthy CNS is thought to not have macrophages; the CNS has cells with a similar lineage called microglia.

1.2.1 Microglia

Microglia are substantial contributors to the overall health of the brain because of their importance as the main immune cells of the CNS and prevalence; microglia comprise 10% of the CNS cellular population [11]. Although microglia are often termed ‘resting’ when they are in their inactive state, inactive microglia are usually mobilizing their appendages to survey their microenvironment [12]. Upon detection of a variety of cues, microglia become activated and take on roles that may be neuroprotective or neurotoxic.

Based on whether activated microglia play a neuroprotective and anti-inflammatory role or a neurotoxic and pro-inflammatory role, they may be classified as M2 or M1, respectively [13]. Dichotomization is an oversimplification following investigation of a variety of molecules, but it may be practical in guiding non-specific anti-inflammatory therapy as microglia may play a variety of roles depending on the molecules that they are expressing. Molecular markers in rats that mark M1 microglia include iNOS, MHCII, and CD68 while those that mark M2 microglia include Arg1, Ym1, and CD206 [14]. Examples of the neuroprotective roles that M2 microglia contribute to are myelin repair, the removal of cellular and protein debris, and the secretion of neurotrophic factors that prevent neural injury [13]. On the other hand, M1 microglia tend to release cytokines that recruit more microglia whilst releasing proteases, reactive nitrogen species, and oxygen species [13].

1.2.2 Astrocytes

Astrocytes are a major cell type in the CNS, and although they are often known for their supportive roles, astrocytes can play a role in inflammatory processes [15]. Supportive roles that astrocytes play include maintenance of synapses, providing energetic metabolites to neurons, forming a key component of the blood-brain-barrier (BBB) along with pericytes and endothelial cells, and

recycling toxic waste products such as ammonia [15]. Like microglia, astrocytes termed A2 exhibit neuroprotective and anti-inflammatory functions such as the support of BBB repair and formation of an astrocytic barrier to restrict the infiltration of other white blood cells whilst releasing signalling molecules that downregulate inflammation [16]. Astrocytes can be termed as A1 when they exhibit neurotoxic and pro-inflammatory functions such as the release of neurotoxic amounts of glutamate whilst releasing signalling molecules that upregulate inflammation [16]. In any case, inflammatory activation of astrocytes can be marked by overexpression of the glial acid fibrillary protein (GFAP) [17]. An important distinction given our interest in WM is that astrocytes are called fibrous or protoplasmic astrocytes based on their appearance and whether they are expressed in WM or grey matter, respectively [17].

1.3 Subcortical Stroke

To contextualize subcortical stroke, it is important to first discuss strokes in general. In the context of the brain, a stroke is when a brain region has insufficient vascular perfusion to survive [18]. Strokes are usually divided into hemorrhagic and ischemic stroke based on whether the stroke is caused by a vascular rupture or occlusion, respectively, as these two require substantially different treatments [18]. Additionally, treatment options in ischemic stroke depend on the time since onset, which has led to the classification of stroke into acute (< 24 hours), subacute (24 hours to 5 days), and chronic (> 5 days) [19]. Alternatively, strokes may be distinguished based on their location, and therefore affected brain functions, into cortical and subcortical strokes [20].

1.3.1 Subcortical Stroke Etiology

According to the Trial of Org 10172 in Acute Stroke Treatment (TOAST) classification, subcortical strokes may be caused by small-vessel disease, large-vessel disease, or embolism [18]. Embolism or large-vessel disease such as arterial stenosis causes subcortical strokes that are larger

than 15 mm in diameter [18]. On the other hand, subcortical strokes associated with small-vessel disease can present as lacunar strokes that are less than 15 mm in diameter and are not caused by embolism or arterial stenosis [18]. In general, lacunar stroke is associated with, and thought to occur by, diffuse abnormality of small vessel endothelial cells, slight increases of BBB permeability, and leakage of substances from the blood that are considered toxic to the brain [21]. Despite evidence for the role of endothelial cells, why lacunar stroke could have a sudden symptomatic onset remains under investigation [21].

1.3.2 Stroke Molecular Changes

Although decreased perfusion triggers the onset of stroke, it is important to realize that there are other downstream toxic effects. In particular, insufficient perfusion in stroke hinders the ability of the affected region to keep up with the demand for energy from adenosine triphosphate, thereby initiating several toxic processes [22]. These include acidosis as the body tries to generate adenosine triphosphate by lactic acid metabolism, glutamate excitotoxicity by induction of calcium and sodium influx and the ensuing edema, production of reactive oxygen species, reactive nitrogen species, lipases, proteases, and nucleases, and activation of glial cells, disruption of the BBB, and infiltration of peripheral leukocytes [22].

1.3.3 Stroke Infarct Core and Penumbra

The concept of infarct core and penumbra is important in stroke and is also relevant in subcortical stroke. The infarct core is a region in the center of the stroke site that is non-functional and does not have enough perfusion to survive. On the other hand, the infarct penumbra is non-functional but, although it has a perfusion deficiency, it can be salvaged using thrombolytic therapy [23]. Salvaging the penumbra improves cognitive and functional outcome in people who experience a stroke [23]. Between people who have lacunar and those with non-lacunar strokes, the incidence

is the same for the detection of an infarct core and penumbra within 4.5 hours, which is 20-60% depending on perfusion thresholds [24].

Rodent studies have shown that the neuroinflammatory cell composition differs between the infarct core and penumbra, but this difference seems to invert with time. Histological differentiation of the infarct core and penumbra may be accomplished using microtubule-associated protein 2 (MAP2) immunohistochemistry signal, which is high in healthy tissue, medium in the infarct penumbra, and low to nonexistent in the infarct core [25,26]. By using multi-label immunofluorescence of neuroinflammatory cells and MAP2 in rodents, a recent study has been able to describe the early post-stroke relationship between the infarct core and penumbra with microglia and astrocytes [27]. In the 2-day re-perfused penumbra, activated astrocytes make a barrier that surrounds the activated M2 microglia-dense infarct core [27]. At later timepoints, activated astrocytes can be mostly found in the center of the infarct while M1 activated microglia tend to be in peripheral regions and remote regions [26–30].

1.3.4 WM Microglial Activation and Disease in Subcortical Stroke

Before describing WM microglial activation, it is necessary to describe the potentially related measurements of WM integrity. WM integrity can be measured with diffusion tensor imaging (DTI), as described below, but the measurements can often have more than one biological interpretation. As one of many magnetic resonance imaging (MRI) techniques, DTI quantifies the rate and directionality of water diffusion. The rate and directionality are represented in the parameters mean diffusivity and fractional anisotropy, respectively. Fractional anisotropy (FA) in particular can be related to WM integrity, with high FA reflecting relatively unimpeded diffusion parallel to the axonal fibers and restricted diffusion perpendicular to the direction of the myelinated axonal fibers [31]. Decreased FA and increased mean diffusivity has been related to a

decrease in myelin content, axon count, and increase in CSF, while the decrease of both FA and mean diffusivity has been interpreted as gliosis, tract incoherence, and a decrease in axon count [31]. Although DTI alone cannot specifically measure myelin content or axon count, changes in FA and mean diffusivity can be interpreted in terms of WM integrity.

Clinical studies of WM disease after subcortical stroke have found that remote regions of the directly affected tract have increased microglial activation and reduced integrity, and that remote WM of tracts that were not directly affected have a late reduction in integrity. In particular, one study showed that remote regions of the directly affected pyramidal tract, which is the major WM tract related to motor function, had increased microglial activation and decreased WM integrity, as indicated by FA, throughout the whole tract at <3 weeks and at 6 months post-stroke [1]. In that study, microglial activation was measured *in vivo* by using PET to take advantage of the increased microglial and astrocyte expression of TSPO. As subcortical strokes outside the non-pyramidal tract had no effect on pyramidal tract microglial activation and integrity, it appeared that the WM tract had to be directly affected by a subcortical stroke for changes in integrity and microglial activation to be detectable by 6 months after stroke in humans. In contrast, the same group found late changes in integrity of a WM region that was not directly affected; the transcallosal motor fiber FA was normal within 20 days but decreased by 6 months after subcortical stroke in the pyramidal tract and not after subcortical stroke outside the pyramidal tract [32]. Overall, this data suggests that subcortical stroke in the pyramidal tract leads to early disintegration of directly connected WM and late disintegration of functionally connected WM. Whether the functionally connected WM experiences microglial activation and whether these findings can be generalized to all subcortical strokes in the pyramidal tract is pending further research.

Leukoaraiosis, also identified as WM hyperintensities using T₂-weighted or fluid-attenuated inversion recovery (FLAIR) MRI, is associated with subcortical lacunar stroke, but not with large subcortical strokes [33]. WM hyperintensities usually refer to leukoaraiosis of presumed vascular etiology, but WM hyperintensities increase with normal aging and may appear due to a variety of pathologies [33,34]. For example, WM hyperintensities have been histologically attributed to various changes such as microglial and astrocyte activation, endothelial activation, edema, vacuolization, demyelination, axonal loss, and the presence of proteins including fibrinogen, immunoglobulins, and thrombomodulin [33]. People with a moderate or severe extent of WM hyperintensity were more likely to have experienced a lacunar stroke than those with mild WM hyperintensities [35]. On the other hand, large subcortical strokes such as striatocapsular stroke are less prevalent in people with WM hyperintensity of a moderate or severe extent compared to mild extent [36].

1.3.5 WM Disease Relationship with Cognition in Subcortical Stroke

There is an established relationship between WM disease and cognition in people with subcortical stroke. In people with lacunar stroke, there is an increasing relationship between executive dysfunction and extent of WM hyperintensities [37]. Moreover, another study found that after a silent lacunar infarct, the reductions in FA in the left external capsule correlated to decreases in memory and language ability [38]. As for large subcortical stroke, a study showed that after 3 months post-stroke, people with a stroke that had a poorer cognitive outcome had reduced FA in several WM regions on the contralateral side, while those with a good cognitive outcome only had reduced FA in the contralateral corpus callosum genu [39]. Overall, this suggests that an increasing load of WM disease after a subcortical stroke often correlates with cognitive decline.

1.4 Alzheimer's Disease (AD)

1.4.1 AD Stages and Diagnosis

AD is a neurodegenerative disease, distinct from subtle cognitive loss associated with aging, characterized by progressive memory loss and the proteopathies of beta-amyloid (A β) and tau. Although the focus of this thesis is WM microglial activation, it is important to discuss the clinical pathogenesis of AD to contextualize our transgenic prodromal AD rat model. In terms of pathogenesis, A β deposits and plaques originate from amyloid precursor protein (APP), which is cleaved into A β monomers that eventually aggregate into deposits and [40]. As for tau, the microtubule-associated protein tau (MAPT) gene produces six splicing isoforms that bind microtubules and may undergo hyperphosphorylation before aggregating into neurofibrillary tangles [41]. Overall, A β and tau are both important diagnostic hallmarks of AD, but A β pathogenesis appears to start before tau pathogenesis. These proteopathies often precede the onset of memory loss, mild cognitive impairment, and mild AD, moderate AD, and severe AD [42,43]. Mild cognitive impairment precedes the progressive loss of memory known as dementia, which is diagnosed based on substantial concern and longitudinal decline in two cognitive domains including memory according to a mental status exam or neuropsychological testing such as the widely used clinical dementia rating. In addition to A β and tau proteopathies, clinical evidence also suggests that WM changes can occur early before cognitive impairment [44].

Although the above stages define the severity of AD, the clinical diagnosis of AD depends on the quality of evidence, which in increasing order can be classified as: possible AD, probable AD, and proven AD (Fig. 1.1) [45]. To give a diagnosis of proven AD, an antemortem diagnosis of possible AD or probable AD needs to be supplemented by post-mortem histopathology showing A β neuritic plaques as scored by the Consortium to Establish a Registry for Alzheimer's disease (CERAD)

and neurofibrillary tau tangles in the neocortex and hippocampus as staged by Braak [46]. A diagnosis of AD may also be supported by post-mortem detection of A β deposits as scored by Thal et al. [47]. Overall, knowing these differences in diagnosis may help explain why some clinical studies differ in their results about the various white matter pathologies.

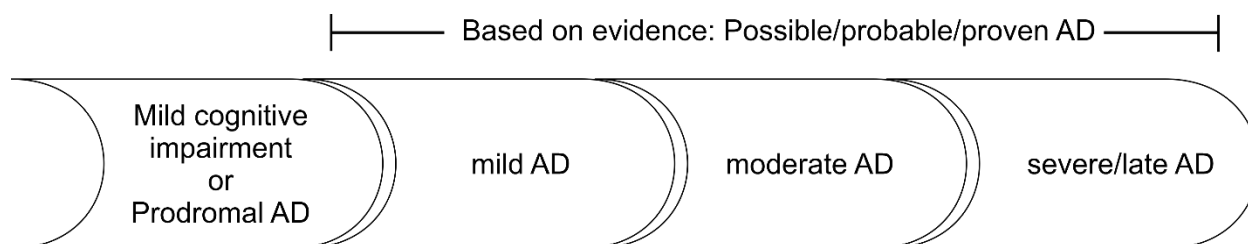


Fig 1.1 AD diagnosis. Diagnosing a stage of AD is based on severity of symptoms, while non-research diagnosis of AD is based on evidence including an AD-like decline of memory (possible AD), absence of other diseases (probable AD), and the histological presence of amyloid and tau (proven AD) [45]

1.4.2 WM Microglial Activation and Disease in AD

Before discussing WM microglial activation in AD, it is important to recognize that neuroinflammation in AD is still a subject of research [48]. In AD, the initial thought was that neuroinflammation only occurs at the site of amyloid deposition. Evidence suggested that excessive accumulation of amyloid induced microglial activation for clearance, which if insufficient led to amyloid deposition and persistent neuroinflammation that had a neurotoxic role [49–52]. Although that explained why neurotoxic activated M1 microglia and A1 astrocytes could be found at the neocortex and hippocampus, in which amyloid is usually deposited, it did not sufficiently explain recent findings that activated M1 microglia can be found in the WM of people with early-onset AD and rat models of prodromal AD [4,53–55].

The presence of WM microglial activation changes is controversial in people with late-onset AD, but early-onset AD seems to have elevated WM microglial activation. To differentiate between early-onset AD and severity of AD, it is important to first discuss Braak staging in detail: Braak staging is often used to define the severity of neurodegenerative diseases using intensity and location of tau pathology; a Braak stage I is often localized to the lower brain stem and the earliest locations where pathology develops while a Braak stage VI has intense tau staining in those early locations and additionally has pathology in other locations including the neocortex [56]. Early-onset AD with severe tau pathology indicated by a Braak stage V-VI has been shown to have elevated WM microglial activation in the transentorhinal cortex and frontal cortex, which according to Braak stages are some of the earliest and latest regions affected in AD respectively [4]. People with early-onset AD and early Braak stages were not investigated, this suggests that WM microglial activation may play a role at least during the late Braak stages of AD pathology. As for people with late-onset AD, histology studies have shown that WM microglial activation is similar between people with late-onset AD and controls [4].

On the other hand, TSPO-PET data of people has been controversial; Kreisl et al. showed normal WM microglial or astrocyte activation in mild cognitive impairment and AD while Suridjan et al. showed elevated WM microglial activation in AD [57,58]. As only Suridjan et al. noted the presence of WM hyperintensities and both studies controlled for TSPO genotype and used structurally similar PET radiotracers, we speculate that an elevated WM microglial or astrocyte activation may be attributed to the presence of lesions or to a late stage of AD [49]. More research is needed to determine the stage at which WM microglial activation appears in humans.

Rodent histological studies by our group have implicated WM microglial activation as an early feature of AD pathology. In particular, we found that a Fischer 344 rat model of prodromal

AD, which overexpresses human Swedish- and Indiana-mutated amyloid precursor protein (TgAPP21) to produce high levels of A β without depositing amyloid plaques, has elevated WM microglial activation that is proportional with age, correlates with executive dysfunction, and is predictive of eventual memory loss [53–55]. Accordingly, WM microglial activation may be related to other disease findings in WM of people with disintegration, demyelination, WM hyperintensities, and atrophy [59–61].

WM integrity as measured by DTI MRI is decreased in people with late AD, but the stage at which disintegration begins remains controversial. By late AD, most evidence supports that WM integrity has deteriorated [62]. In contrast, the evidence for earlier stages is conflicted. For example, a 1-year longitudinal and cross-sectional study by Nowrangi et al. showed that the most commonly used DTI measurement FA was and remained similar between healthy controls and people with mild cognitive impairment. There was an observed increase in the other DTI measurement of mean diffusivity, which the authors attributed to loss of neurons, axons, and dendrites, in people with mild cognitive impairment [61]. On the other hand, a study with a 2-year follow up by Zhuang et al. found that FA was initially lower in 16 people who were normal converted to amnesic cognitive impairment compared to 173 people who remained cognitively normal [44]. To resolve this conflict, a longitudinal study with a larger sample size is necessary and is expected to be provided by the Alzheimer's Disease Neuroimaging Initiative [63].

WM demyelination has also been detected throughout the course of AD using the myelin-sensitive MRI measurement, magnetization transfer ratio (MTR). Magnetization transfer imaging can use the transfer of magnetization between protons of free water and those bound to macromolecules to measure MTR, which corresponds to myelin in WM. In one study, reduced MTR was detected in mild cognitive impairment and AD using a voxel histogram peak analysis,

but this was not detectable using mean MTR [64]. The limited reduction in MTR might imply that mild cognitive impairment represents an AD stage at which WM demyelination has not fully occurred. In late AD, the loss of myelin has been histologically confirmed using Luxol fast blue staining [65].

1.5 Measuring WM Microglial Activation

Given the importance of WM in neuronal communication and the observation that microglial activation can have deleterious effects, it is important to study microglial activation in the WM. Amongst the many molecules that can mark microglial activation, our interests are in the major histocompatibility complex (MHC) class II molecules and translocator protein (TSPO).

1.5.1 Major Histocompatibility Complex Class II (MHCII) Molecules

MHCII molecules are important in adaptive immunity and often measured to study WM microglial activation in multiple sclerosis and AD. MHCII molecules are a group of molecules that are expressed by the MHCII region of the genome in organisms that have them, and include those that have a structure made up of an alpha chain and beta chain folding together to integrate in lipid membranes and make an extracellular domain for presenting antigens to other cells. A well studied example of this is the presentation of antigens to the T-cell receptor on CD4+ T cells, which is a type of adaptive immunity that could also have cytotoxic effects when activated [66]. In people with early-onset AD, a recent study has also demonstrated with immunohistochemistry (IHC) that microglial activation and MHCII molecules are increased in the WM [4]. Given observations of activated MHCII microglia in the WM of early-onset AD and the potential cytotoxic effects of MHCII molecules, MHCII molecules are compelling markers of WM microglial activation.

1.5.2 Translocator Protein (TSPO)

As mentioned in earlier sections, TSPO-PET has been used to observe chronic WM inflammation in people with subcortical stroke and people with AD [1,58]. This makes it an ideal candidate for *in vivo* imaging of chronic WM MHCII microglial activation.

TSPO was discovered as a variant of the central benzodiazepine receptor that had differences in ligand binding and was expressed in the kidney, which led to its initial name peripheral benzodiazepine receptor (PBR) [67]. PBR was renamed to TSPO because of its implication in the intracellular movement of cholesterol, but some authors have stated that this lacks sufficient experimental proof [68,69]. Nevertheless, TSPO has been implicated in a variety of functions and as a marker of neuroinflammation [70].

Neuroinflammatory expression of TSPO has been mostly attributed to activated microglia and, in some studies, activated astrocytes. Initial studies of rat brains reported that TSPO expression could be attributed to activated microglia and astrocytes [71,72]. Recent studies have suggested that TSPO is not expressed by astrocytes [73,74]. Astrocyte expression of TSPO may be circumstantial as stroke studies of TSPO have shown that the number of astrocytes expressing TSPO increases with time after a stroke [28,75,76].

1.6 Positron Emission Tomography (PET)

Although MRI can quantify WM integrity, demyelination, hyperintensities, and the core and penumbra of a stroke, it cannot specifically measure microglial activation. WM microglial activation can, however, be measured in living subjects using TSPO-PET. In this thesis, the main objective was to determine whether TSPO-PET can detect WM microglial activation that is marked by MHCII. Accordingly, the follow sections provide background on PET.

PET radiotracer production typically begins with a cyclotron that accelerates a positively charged particle into a target to produce positron-emitting radioisotopes. Positron-emitting radioisotopes such as ^{18}F and ^{11}C , which have a half-life of 109.7 and 20.4 mins respectively, are incorporated into exogenous agents with high affinity and specificity for the targeted molecule. When in the subject, the radiolabeled molecules accumulate at the regions of interest and emit high energy positrons that annihilate with nearby electrons to produce two antiparallel photons at an energy of 511 keV. These gamma rays exit the body to the PET scanner, where they are detected in coincidence and converted into a signal by a ring of scintillator arrays that is optically coupled to photodetectors.

The acquired signal is stored in list-mode data set (containing detector locations and detection time for each coincidence event), processed into sinograms, and reconstructed into volumes portraying the distribution of PET tracer averaged over a period of time in a single frame or multiple frames. For a 3D acquisition, each frame of data can be binned into a set of N^2 oblique sinograms between detector rings, where N is the number of detector rings and a sinogram is a graph that plots the number of coincidences detected for each possible detector pair [77]. Sinograms are corrected for random and scatter emission events before PET images are reconstructed using a filtered back projection reconstruction or iteratively by comparing them to the sinograms of different theoretical volumes. For example, the iterative reconstruction algorithm used in chapter 2, 3D ordered-subset expectation maximization followed by fast maximum *a posteriori* (OSEM3D/FMAP), works by dividing the measured sinograms into non-overlapping subsets and using only one subset at a time to minimize the difference between the measured subset and a theoretical subset that is based on the forward projection of a model image (OSEM3D), and then by maximizing a function that penalizes images that do not fit the data well (MAP) [78,79].

1.6.1 PET Spatial Resolution

As producing a PET volume requires information about detector location, detector size is inversely related to resolution, but it is also directly related to sensitivity. In other words, decreasing detector sizes could increase resolution by providing a better estimate of where gamma rays strike the PET instrument, but sensitivity would decrease as the detectors might become too small to detect a sufficient number of photons.

System resolution is also limited by positron physics. For one, before annihilating with electrons to produce two 511 keV gamma rays, positrons can diffuse for a distance related to their maximum emission energy. The uncertainty about where the positrons were emitted poses a resolution limit. Second, resolution is limited because the produced gamma rays are not perfectly anti-parallel if the positron has residual momentum, which results in an angle that ranges from 179.75° and 180.25° , which means that there is a range for where the annihilation could have happened. To reduce the range, the diameter of the bore could be decreased, but this is only feasible up to a limit. Overall, the resolution of any PET system is physically limited by the distance a positron could diffuse before annihilating and the fact that the produced gamma rays are not always perfectly anti-parallel.

1.6.2 Radiotracer Target, Sensitivity, and Specificity

Radiotracers may be divided based on their target reaction and kinetic behavior. Target reactions guide the initial process of radiotracer development; for the development of radiotracer to be worthwhile, it has to have clinically meaningful implications. Example reactions include physiological processes such as perfusion or blood-tissue exchange, but the majority of PET tracers developed target a protein [80]. Based on their kinetic behavior, radiotracers may be further divided into those that are reversible and irreversible [81]. Reversible radiotracers are able to

achieve equilibrium by the end of an experiment while irreversible radiotracers generally do not achieve equilibrium. An example of an irreversible radiotracer is [^{11}C]deprenyl, which binds by making a covalent bond with its target protein monoamine-oxidase B to estimate CNS amine breakdown such as that of dopamine [82]. Although an irreversible radiotracer is generally thought to be advantageous because it simplifies analysis, it can be disadvantageous by having limited sensitivity in regions of high target concentrations when there are insufficient amounts of radiotracer to saturate the targets [82].

Sensitivity of PET radiotracers refers to their affinity to the target reaction, such as binding for neuroreceptor radiotracers and delivery for flow radiotracers, and can be validated *in vitro*, *ex vivo*, and *in vivo*. Affinity to the target reaction is a practical concept for quantifying how effectively the radiotracer could detect the target reaction. For reversibly binding tracers, *in vitro* samples containing the target are usually subject to competitive binding assays as part of the initial validation of a radiotracer [83]. Later studies may validate *in vivo* binding affinity by injecting a cold competitive binder in experiments of blocking or displacement, but this is not feasible for all target reactions. For example, blocking or displacement studies are not feasible for TSPO because an unsafe concentration of cold binding molecules is required to saturate the many TSPO binding sites in the body [84].

PET radiotracer specificity is one of the most prevalent reasons for why radiotracers fail, and although there are *in vitro* approaches to quantify specificity, they do not always correspond to *in vivo* results. Radiotracers often fail *in vivo* because they bind to off-target proteins or lipids, which could have misleading consequences. Ideally, *in vitro* tests would have been conducted to evaluate radiotracer specificity. For brain studies, a high lipophilicity of the radiotracer often corresponds to high nonspecific binding [83]. Nevertheless, radiotracers could have low

lipophilicity and still demonstrate nonspecific binding *in vivo*; in these cases, competitive binding experiments that can quantify sensitivity show a high PET signal after injection of the competitive molecule.

1.6.3 Tracer Kinetic Modelling

Tracer kinetic modelling has the practical purpose of condensing dynamic information into quantities of the primary processes that affect tracer distribution. PET experiments can produce a lot of dynamic information because, after being injected into a subject, tracers do not instantaneously get distributed according to the quantity of the target reaction. Instead, the tracer dynamically experiences two or more processes including delivery, clearance, and the target reaction. As a result, the tracer undergoes dynamic change, and this can be seen by plotting the tracer radioactivity against time to construct what is frequently referred to as a time-activity-curve. Although for an ideal radiotracer, an estimate of the target reaction may be semi-quantified using a single late timepoint activity measurement such as standardized uptake value (SUV) normalized to the injected dose and subject weight or the later-discussed reference region-based uptake ratio (UR - often called SUVR), it is possible to use tracer kinetic modelling to obtain an exact rate measurement of the target reaction, delivery, clearance and other reactions or processes. By condensing a lot of information into exact rate measurements, tracer kinetic modelling serves a practical purpose.

The types of rates and their interpretation depend on the chosen tracer kinetic model. Although more complicated models can be more informative, they are computationally demanding to solve and, more importantly, often less robust.

1.6.3.1 Compartmental Modelling

Compartmental models are well-suited to maximize the current abilities of PET. Compartmental tracer kinetic models are based on how the rate of reactions are linearly related to their rate constant and substrate concentration, which may be considered uniform using conceptual compartments such as states, locations, or their combination. In reality, there are many theoretical tracer compartments, but the ability to resolve them are limited by current insufficiencies in PET including signal, resolution, and the inability to distinguish radioactivity sources [85]. Instead, these PET insufficiencies and the ability to make uniformity assumptions dictate whether a compartment is resolvable. In doing so, compartmental models maximize the number of practical parameters that can be accurately extracted from PET data.

The 2TCM provides the highest number of parameters that are usually solved for in PET studies. It is based on the distinction of two tissue compartments: a nondisplaceable compartment (C_1) that is in equilibrium with the bound compartment (C_2), with a tracer-dependent distinction between a plasma compartment (C_p) and a blood compartment (C_b). Having been designed for tracers with slow reversible reactions, the 2TCM has 5 microparameters: K_1 = plasma-to-nondisplaceable-compartment transfer rate (delivery), k_2 = nondisplaceable-compartment-to-plasma transfer rate (clearance), k_3 = nondisplaceable-compartment-to-target-compartment transfer rate, k_4 = target-compartment-to-nondisplaceable-compartment transfer rate, and V_b = blood volume fraction (Fig. 1.2) [86]. Each of these parameters has an important clinical relevance. Namely, K_1 equates to the product of blood flow and tracer extraction fraction, the latter of which is related to permeability of the BBB in PET studies of the brain. Both of these measurements could be affected by a pathology. On the other hand, k_2 is related to K_1 ; if blood flow changes K_1 , k_2 rapidly compensates for the change [87,88]. V_b is relatively straightforward; a pathology could

change the blood-volume fraction. Lastly, k_3 and k_4 correspond to the *in vivo*- and tracer-dependent rate estimates of association with the available target protein and its reversal, respectively. As these two rate estimates are related to the amount of the target molecule, which should have a clinically significant interpretation, the 2TCM is usually used when possible.

An important requirement of the 2TCM is that it requires invasive blood sampling and metabolite fractionation to determine the fraction of non-metabolized radiotracer in the plasma (C_p) and the blood compartment (C_b). This is because radiotracers can be metabolized and the metabolites cannot be differentiated from the parent by the PET detector. To model only the parent, its fraction in the arterial blood is required. Given the invasive nature of arterial sampling, non-invasive methods to derive the input function are actively being pursued [89,90].

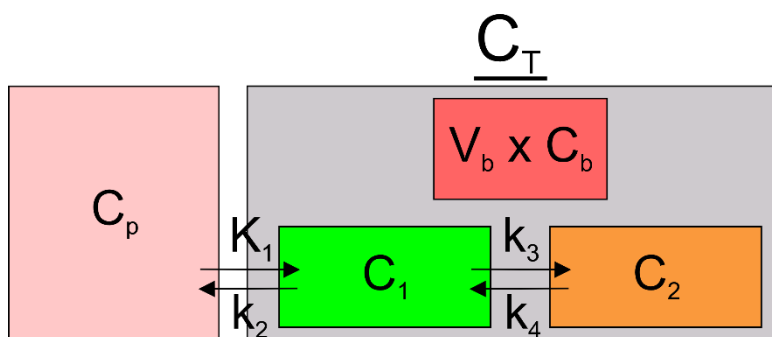


Fig 1.2 A visual representation of a 2TCM. In this model, the plasma pool (C_p) is distinguished from the whole blood pool (C_b). When the whole blood pool is multiplied by the volume fraction of tissue that is occupied by blood vessels (V_b), the blood-sourced activity ($V_b \times C_b$) can be separated from the rest of the tissue (C_1 and C_2), which all together makes up the detector-measured C_T as defined in Eq 1.3. The radiotracer gets exchanged and eventually achieves equilibrium between C_p and C_1 , and between C_1 and C_2 . The rates at which the parent radiotracer is exchanged between compartments are indicated using K_1 (delivery), k_2 (clearance), k_3 (binding), and k_4 (unbinding)

Compartmental models are often solved using the nonlinear least-squares approach, but this can produce inaccurate microparameters [91,92]. The approach continually alters parameters of a simulated curve until it matches the measured curve as guided by numerical curve differences

and, usually, derivative-based algorithms. Unfortunately, derivative-based algorithms require an accurate initial estimate to converge to the global optimum as there can be more than one local optimum, which is the result of noise and inversely correlated model parameters [91,93]. As nonlinear least-squares algorithms are more likely to find the global optimum if the parameter search space is smaller, most studies eliminate one dimension by fixing V_b to a predetermined value. Another way to reduce the number of dimensions can be used for the 2TCM; blocking or displacement experiments may be used to simulate a scenario where k_3 and k_4 are equal to zero, but as mentioned earlier, these are not feasible for all PET targets. On the other hand, the parameters may also be reduced by setting k_3 and k_4 to zero, which is valid if the tracer kinetics may effectively be modeled with a single tissue compartment model (1TCM) when the tracer does not have a target reaction beyond delivery or if the target reaction rapidly achieves equilibrium [94]. Overall, the inability to estimate the initial target parameters and the local minimum problem make it challenging for the nonlinear least-squares-fitting approach to prove that the converged parameters are the true parameters [95].

1.6.3.2 Total Distribution Volume (V_T)

Regardless of method, most PET papers that use tracer kinetic modelling on reversible binding ligands report the robust but aggregated macroparameter V_T . V_T is defined as the equilibrium ratio of radiotracer concentration in the region of interest, not including the blood component, to that in plasma (Eqs. 1.1 and 1.2). A downside to this definition is that V_T largely consists of the equilibrium concentration in the non-displaceable compartment, making V_T an aggregated macroparameter that is not purely representative of the target binding reaction. On the other hand, this activity-ratio-based definition allows for robust calculation of V_T ; V_T will be accurate if the measured curve reasonably matches the fitted curve, which can be done using the 1TCM or 2TCM

(equations below). Overall, despite V_T being an aggregated macroparameter that contains information about the non-displaceable compartment, its activity-ratio definition makes it a robust parameter to report.

Eq 1.1 (1TCM):
$$V_T = \frac{K_1}{k_2}$$

Eq 1.2 (2TCM):
$$V_T = \frac{K_1}{k_2} \left(1 + \frac{k_3}{k_4} \right)$$

1.5.3.3 Logan Graphical Analysis

Logan graphical analysis is one of the most widely used methods for determining V_T of reversibly binding tracers. It started in 1990, when Patlak's work on graphical analysis of non-reversible tracers inspired Logan to extend the work to reversible tracers [96]. At the time, Logan graphical analysis provided a method to solve V_T that was computationally simple, robust, and does not require the specification of a compartmental model; although based on compartment models, differentiating between them does not change the slope on the graphical analysis and therefore distribution volume. Improvements in PET signal-to-noise ratio have increased the robustness of Logan graphical analysis by correcting earlier underestimates of V_T [97]. Given this improvement in signal-to-noise ratio, the simplicity, and model-independence of Logan graphical analysis, it is no surprise that Logan graphical analysis is still one of the most widely used methods for calculating V_T .

Logan graphical analysis follows the simple linear regression equation $Y = \text{slope} \cdot X + \text{intercept}$. Although Logan analysis is model-independent, the interpretation of the slope and intercept depends on the model and assumptions. For a 2TCM that distinguishes between the concentration of radioactivity in total blood and the concentration of free parent metabolite in the

plasma, a full solution is provided in Appendix A. Briefly, the model, assumptions, and solution are as follows:

$$\text{Eq 1.3:} \quad C_T(t) = C_1(t) + C_2(t) + V_b C_B(t)$$

$$\text{Eq 1.4:} \quad \frac{dC_1(t)}{dt} = K_1 C_p(t) - k_2 C_1(t) - k_3 C_1(t) + k_4 C_2(t)$$

$$\text{Eq 1.5:} \quad \frac{dC_2(t)}{dt} = k_3 C_1(t) - k_4 C_2(t)$$

$$\text{Eq 1.6:} \quad \frac{\int_0^t C_T(u) du}{C_T(t)} = V_T \frac{\int_0^t C_p(u) du}{C_T(t)} - \frac{1}{k_2} \left(1 + \frac{k_3}{k_4}\right) + V_b \left(1 + \frac{1}{k_2} + \frac{k_3}{k_4 k_2}\right) \frac{\int_0^t C_B(u) du}{C_T(t)} - \left(\frac{1}{k_4}\right) \frac{C_2(t)}{C_T(t)}$$

Where for reversible tracer binding in a 2TCM:

$$V_T = \frac{K_1}{k_2} \left(1 + \frac{k_3}{k_4}\right)$$

C_T = Concentration of total radioactivity in the tissue

C_p = Concentration of free parent metabolite in the plasma

C_B = Concentration of total radioactivity in whole blood

C_1 = Concentration of parent metabolite in the non-displaceable compartment

C_2 = Concentration of parent metabolite in the bound compartment

V_b = The ROI volume fraction of vascular tissue

K_1 = plasma-to-unbound-compartment transfer rate (delivery)

k_2 = unbound-compartment-to-plasma transfer rate (clearance)

k_3 = unbound-compartment-to-bound-compartment transfer rate (binding)

k_4 = bound-compartment-to-unbound-compartment transfer rate (unbinding)

1.6.4 Reference Regions

In PET studies, reference regions techniques make quantification convenient because they omit the need for invasive blood sampling and microparameter fitting. Blood sampling can be avoided when using reference regions techniques because they omit the need for concentration of free parent metabolite in the plasma, the obtaining of which (i) is invasive because it requires catheterization for blood samples and (ii) labor-intensive and error-prone because it requires methods for extracting metabolite fractions from blood samples. An example of such a technique is the semi-quantitative uptake ratio approach (UR), which relies on the assumption that there are no unmetabolized radioligands in the reference region. Additionally, to determine the important ratio of radiotracer concentration in the specifically bound compartment to that in the nondisplaceable compartment (BP_{ND}), error-prone microparameter fitting can be avoided by using reference regions and the Logan V_T -based reference region techniques (equation below). This requires the assumption that the reference region is physiologically identical to the region of interest except for the target reaction(s) being quantified, which in the reference region should be nonexistent. Therefore, given the right assumptions, reference region techniques are convenient because they allow the determination of BP_{ND} without error-prone microparameter fitting and, also for determining the semi-quantitative UR, without blood sampling and metabolite analysis.

$$\text{Eq. 1.7: } BP_{ND}(ROI) = \frac{V_S(ROI)}{V_{ND}(ROI)} = \frac{V_T(ROI) - V_{ND}(ROI)}{V_{ND}(ROI)} = \frac{V_T(ROI) - V_T(Ref)}{V_T(Ref)} = \frac{k_3}{k_4}$$

Where V_s is the distribution volume in the bound compartment and V_{ND} is the distribution volume in the nondisplaceable compartment

1.6.5 Ex Vivo PET Validation

Quantitative validations of PET are usually done using the *ex vivo* methods of autoradiography and western blotting. Relative to PET, autoradiography allows validation of the PET radiotracer at a higher resolution and, importantly, simpler binding context. The higher resolution is derived by placing tissue sections incubated with radiotracer closer to high-resolution detectors than possible with PET. Analysis of binding is simplified because (i) the radiotracer does not need to pass a blood compartment, (ii) equilibrium can be achieved rapidly, and (iii) the non-specific binding can be assessed using non-radioactive ligands at toxic concentrations [98]. In contrast, western blotting resolution is technically limited, but it can produce pure quantitative measurements of the target protein amount. The user must sample a region of interest, homogenize it, separate it in a gel, incubate it with a target-protein-binding chromogenic antibody complex, then use the amount of signal it emits to quantify protein amount by regression from predetermined quantities of standard proteins [99]. Overall, autoradiography provides high resolution of radiotracer binding while western blotting provides accurate quantities of the target protein without the need to quantify binding constants.

1.6.5.1 Immunohistochemistry (IHC)

IHC provides a very high resolution of the target protein, but the measurements are semi-quantitative. Briefly, IHC is when tissue sections are incubated with a chromogenic antibody complex that can be imaged with high-resolution microscopes. IHC resolution is much higher than PET because (i) the chromogen is near the target protein and (ii) the physical laws that limit microscopy are much less restrictive. Unfortunately, traditional IHC is semi-quantitative and restricted to counting or area coverage analysis because the protein-to-signal relationship is not perfectly proportional. This is mainly because the binding between protein antigen and antibodies

is not stoichiometric but can also be attributed to chromogens that do not follow Beer-Lambert's law. All together, although IHC is semi-quantitative, the process and physical laws give it a much higher resolution than PET.

1.6.6 TSPO-PET

Given the ability of TSPO to mark activated microglia that was mentioned in section 1.5.2, and the knowledge of ligands that can bind TSPO, many TSPO-targeting radiotracers have been developed to quantify microglial activation *in vivo* [100]. Initial radiotracers included those based on benzodiazepines such as [¹¹C]Ro5-4864 and isoquinoline carboxamides such as [¹¹C]PK11195. In a later generation, [¹¹C]Ro5-4864 binding inspired the development of [¹¹C]DAA1106 and other phenoxy acetamides with high binding affinity such as [¹¹C]PBR28 and [¹⁸F]FEPPA. New radiotracers for TSPO continue to be developed because of quantification issues.

TSPO-PET quantification has been hindered by low binding specificity in the initial radiotracer [¹¹C]PK11195, sensitivity to human polymorphisms in newer generation tracers, and the absence of a true reference region. The first PET tracer was [¹¹C]PK11195, but its low binding specificity limited the signal-to-noise ratio of true TSPO expression [101]. Binding specificity was improved in newer generation PET tracers, but they proved sensitive to TSPO human polymorphisms and therefore additionally required a genetic analysis for accurate quantification [102]. This polymorphism sensitivity initially seemed solved by [¹⁸F]GE180 and the yet newer radiotracer [¹¹C]ER176, but these were later revealed to be artifacts or did not translate from *in vitro* studies to *in vivo* studies respectively [103,104]. Finally, the absence of a true reference region that is devoid of TSPO expression has made it technically challenging to quantify PET tracer uptake [105].

1.7 Rationale and Objectives

AD and subcortical stroke are both common neurological diseases with unfortunate cognitive prognoses. Although their main pathologies are different, WM microglial activation and other WM abnormalities are key components to the pathogenesis of both AD and stroke. Specifically, our group has used preclinical co-morbid rodent models of disease to demonstrate that diffuse WM microglial activation increases with normal age, is accelerated in transgenic AD rats and following subcortical stroke, associates with executive dysfunction, and is predictive of learning and memory impairment [29,30,53,55,106].

To longitudinally measure cognitive function and WM microglial activation, there is a need for an *in vivo* imaging modality that can image WM microglial activation. As TSPO-PET can quantify microglial activation and has been used to observe chronic WM inflammation in subcortical stroke and AD, we hypothesized that the chronic WM microglial activation that is histochemically detected using MHCII in our subcortical stroke and prodromal AD rat models can also be detected using TSPO-PET. To test this hypothesis, this thesis had the following objectives:

1. To investigate WM microglial activation in a rat model of prodromal AD with TSPO-PET using the 2nd generation radiotracer, [¹⁸F]FEPPA.
2. To investigate WM microglial activation longitudinally in a rat model of subcortical stroke with TSPO-PET.
3. To investigate and validate WM TSPO expression in a rat model of subcortical stroke at 7-days and 28-days using IHC.
4. To investigate WM microglial and astrocyte activation in a rat model of subcortical stroke using MHCII, iNOS, and GFAP IHC at 7-days and 28-days post-stroke.
5. To compare TSPO-PET and TSPO IHC to MHCII IHC.

Results from these studies are reported in Chapter 2, which is currently under review for publication in the journal *European Journal of Nuclear Medicine and Molecular Imaging (EJNMMI) Research*.

1.8 References

1. Thiel A, Radlinska BA, Paquette C, et al. The temporal dynamics of poststroke neuroinflammation: a longitudinal diffusion tensor imaging-guided PET study with ¹¹C-PK11195 in acute subcortical stroke. *J Nucl Med*. 2010;51:1404-1412.
2. Johnson VE, Stewart JE, Begbie FD, Trojanowski JQ, Smith DH, Stewart W. Inflammation and white matter degeneration persist for years after a single traumatic brain injury. *Brain*. 2013;136:28-42.
3. Chiappelli J, Hong LE, Wijtenburg SA, et al. Alterations in frontal white matter neurochemistry and microstructure in schizophrenia: implications for neuroinflammation. *Transl Psychiatry*. 2015;5:e548-e548.
4. Raj D, Yin Z, Breur M, et al. Increased White Matter Inflammation in Aging- and Alzheimer's Disease Brain. *Front Mol Neurosci*. 2017;10:206.
5. Subramaniam SR, Federoff HJ. Targeting Microglial Activation States as a Therapeutic Avenue in Parkinson's Disease. *Front Aging Neurosci*. 2017;9:176.
6. Hoogenraad CC, Wierenga C. Neurons, Overview. In: Aminoff MJ, Daroff RB, eds. *Encyclopedia of the Neurological Sciences (Second Edition)*. Oxford: Academic Press; 2014:456-458.
7. Waxman SG. Conduction in Myelinated, Unmyelinated, and Demyelinated Fibers. *Arch Neurol*. 1977;34:585-589.
8. Feghali CA, Wright TM. Cytokines in acute and chronic inflammation. *Front Biosci*. 1997;2:d12-26.
9. Aderem A, Underhill DM. Mechanisms of Phagocytosis in Macrophages. *Annu Rev Immunol*. 1999;17:593-623.
10. Mirza R, DiPietro LA, Koh TJ. Selective and specific macrophage ablation is detrimental to wound healing in mice. *Am J Pathol*. 2009;175:2454-2462.
11. DiSabato D, Quan N, Godbout JP. Neuroinflammation: The Devil is in the Details. *J Neurochem*. 2016;139:136-153.
12. Nimmerjahn A, Kirchhoff F, Helmchen F. Resting microglial cells are highly dynamic surveillants of brain parenchyma in vivo. *Science*. 2005;308:1314-1318.
13. Tang Y, Le W. Differential Roles of M1 and M2 Microglia in Neurodegenerative Diseases. *Mol Neurobiol*. 2016;53:1181-1194.
14. Hu Xiaoming, Li Peiying, Guo Yanling, et al. Microglia/Macrophage Polarization Dynamics Reveal Novel Mechanism of Injury Expansion After Focal Cerebral Ischemia. *Stroke*. 2012;43:3063-3070.

15. Weber B, Barros LF. The Astrocyte: Powerhouse and Recycling Center. *Cold Spring Harb Perspect Biol.* 2015;7.
16. Faulkner JR, Herrmann JE, Woo MJ, Tansey KE, Doan NB, Sofroniew MV. Reactive astrocytes protect tissue and preserve function after spinal cord injury. *J Neurosci.* 2004;24:2143-2155.
17. Sofroniew MV, Vinters HV. Astrocytes: biology and pathology. *Acta Neuropathol (Berl).* 2010;119:7-35.
18. Adams HP, Bendixen BH, Kappelle LJ, et al. Classification of subtype of acute ischemic stroke. Definitions for use in a multicenter clinical trial. TOAST. Trial of Org 10172 in Acute Stroke Treatment. *Stroke.* 1993;24:35-41.
19. Birenbaum D, Bancroft LW, Felsberg GJ. Imaging in Acute Stroke. *West J Emerg Med.* 2011;12:67-76.
20. Venkataraman P, Tadi P, Lui F. Lacunar Syndromes. In: *StatPearls.* Treasure Island (FL): StatPearls Publishing; 2020.
21. Wardlaw JM. What causes lacunar stroke? *J Neurol Neurosurg Psychiatry.* 2005;76:617-619.
22. Xing C, Arai K, Lo EH, Hommel M. Pathophysiologic Cascades in Ischemic Stroke. *Int J Stroke.* 2012;7:378-385.
23. Kidwell CS, Saver JL, Mattiello J, et al. Thrombolytic reversal of acute human cerebral ischemic injury shown by diffusion/perfusion magnetic resonance imaging. *Ann Neurol.* 2000;47:462-469.
24. Rudilosso S, Urra X, Román LS, et al. Perfusion Deficits and Mismatch in Patients with Acute Lacunar Infarcts Studied with Whole-Brain CT Perfusion. *Am J Neuroradiol.* 2015;36:1407-1412.
25. Kharlamov A, LaVerde GC, Nemoto EM, et al. MAP2 immunostaining in thick sections for early ischemic stroke infarct volume in non-human primate brain. *J Neurosci Methods.* 2009;182:205-210.
26. Popp A, Jaenisch N, Witte OW, Frahm C. Identification of ischemic regions in a rat model of stroke. *PloS One.* 2009;4:e4764.
27. Buscemi L, Price M, Bezzi P, Hirt L. Spatio-temporal overview of neuroinflammation in an experimental mouse stroke model. *Sci Rep.* 2019;9:507.
28. Wang Y, Yue X, Kiesewetter DO, et al. [18F]DPA-714 PET Imaging of AMD3100 Treatment in a Mouse Model of Stroke. *Mol Pharm.* 2014;11:3463-3470.

29. Weishaupt N, Zhang A, Deziel RA, Tasker RA, Whitehead SN. Prefrontal Ischemia in the Rat Leads to Secondary Damage and Inflammation in Remote Gray and White Matter Regions. *Front Neurosci.* 2016;10.
30. Weishaupt N, Riccio P, Dobbs T, Hachinski VC, Whitehead SN. Characterization of Behaviour and Remote Degeneration Following Thalamic Stroke in the Rat. *Int J Mol Sci.* 2015;16:13921-13936.
31. Madden DJ, Bennett IJ, Burzynska A, Potter GG, Chen N, Song AW. Diffusion tensor imaging of cerebral white matter integrity in cognitive aging. *Biochim Biophys Acta BBA - Mol Basis Dis.* 2012;1822:386-400.
32. Radlinska BA, Blunk Y, Leppert IR, Minuk J, Pike GB, Thiel A. Changes in Callosal Motor Fiber Integrity after Subcortical Stroke of the Pyramidal Tract. *J Cereb Blood Flow Metab.* 2012;32:1515-1524.
33. Wardlaw JM, Valdés Hernández MC, Muñoz-Maniega S. What are White Matter Hyperintensities Made of? *J Am Heart Assoc Cardiovasc Cerebrovasc Dis.* 2015;4.
34. Wardlaw JM, Smith EE, Biessels GJ, et al. Neuroimaging standards for research into small vessel disease and its contribution to ageing and neurodegeneration. *Lancet Neurol.* 2013;12:822-838.
35. Basile AM, Pantoni L, Pracucci G, et al. Age, Hypertension, and Lacunar Stroke Are the Major Determinants of the Severity of Age-Related White Matter Changes. *Cerebrovasc Dis.* 2006;21:315-322.
36. Held V, Szabo K, Bänzner H, Hennerici MG. Chronic Small Vessel Disease Affects Clinical Outcome in Patients with Acute Striatocapsular Stroke. *Cerebrovasc Dis.* 2012;33:86-91.
37. Wen HM, Mok VCT, Fan YH, et al. Effect of white matter changes on cognitive impairment in patients with lacunar infarcts. *Stroke.* 2004;35:1826-1830.
38. Chen Y, Wang A, Tang J, et al. Association of white matter integrity and cognitive functions in patients with subcortical silent lacunar infarcts. *Stroke.* 2015;46:1123-1126.
39. Dacosta-Aguayo R, Graña M, Fernández-Andújar M, et al. Structural integrity of the contralesional hemisphere predicts cognitive impairment in ischemic stroke at three months. *PloS One.* 2014;9:e86119.
40. Sperling RA, Aisen PS, Beckett LA, et al. Toward defining the preclinical stages of Alzheimer's disease: Recommendations from the National Institute on Aging-Alzheimer's Association workgroups on diagnostic guidelines for Alzheimer's disease. *Alzheimers Dement.* 2011;7:280-292.
41. Caillet-Boudin M-L, Buée L, Sergeant N, Lefebvre B. Regulation of human MAPT gene expression. *Mol Neurodegener.* 2015;10:28.

42. Brunnström HR, Englund EM. Cause of death in patients with dementia disorders. *Eur J Neurol*. 2009;16:488-492.
43. Jack CR, Knopman DS, Jagust WJ, et al. Tracking pathophysiological processes in Alzheimer's disease: an updated hypothetical model of dynamic biomarkers. *Lancet Neurol*. 2013;12:207-216.
44. Zhuang L, Sachdev PS, Trollor JN, et al. Microstructural white matter changes in cognitively normal individuals at risk of amnesic MCI. *Neurology*. 2012;79:748-754.
45. McKhann GM, Knopman DS, Chertkow H, et al. The diagnosis of dementia due to Alzheimer's disease: Recommendations from the National Institute on Aging-Alzheimer's Association workgroups on diagnostic guidelines for Alzheimer's disease. *Alzheimers Dement*. 2011;7:263-269.
46. Hyman BT, Trojanowski JQ. Editorial on Consensus Recommendations for the Postmortem Diagnosis of Alzheimer Disease from the National Institute on Aging and the Reagan Institute Working Group on Diagnostic Criteria for the Neuropathological Assessment of Alzheimer Disease. *J Neuropathol Exp Neurol*. 1997;56:1095-1097.
47. Hyman BT, Phelps CH, Beach TG, et al. National Institute on Aging-Alzheimer's Association guidelines for the neuropathologic assessment of Alzheimer's disease. *Alzheimers Dement*. 2012;8:1-13.
48. Heppner FL, Ransohoff RM, Becher B. Immune attack: the role of inflammation in Alzheimer disease. *Nat Rev Neurosci*. 2015;16:358-372.
49. McGeer PL, McGeer EG. Inflammation, autotoxicity and Alzheimer disease. *Neurobiol Aging*. 2001;22:799-809.
50. McGeer PL, Itagaki S, Tago H, McGeer EG. Reactive microglia in patients with senile dementia of the Alzheimer type are positive for the histocompatibility glycoprotein HLA-DR. *Neurosci Lett*. 1987;79:195-200.
51. McGeer PL, Rogers J, McGeer EG. Inflammation, anti-inflammatory agents and Alzheimer disease: The last 12 years. *J Alzheimers Dis*. 2006;9:271-276.
52. Liddel SA, Guttenplan KA, Clarke LE, et al. Neurotoxic reactive astrocytes are induced by activated microglia. *Nature*. 2017;541:481-487.
53. Levit A, Regis AM, Gibson A, et al. Impaired behavioural flexibility related to white matter microgliosis in the TgAPP21 rat model of Alzheimer disease. *Brain Behav Immun*. 2019:25-34.
54. Levit A, Allman BL, Nagalingam R, Hachinski V, Whitehead S. Age-dependent white matter inflammation and cognitive impairment in the TgAPP21 rat model of Alzheimer disease. *Neurology*. 2018;91:242-242.

55. Weishaupt N, Liu Q, Shin S, et al. APP21 transgenic rats develop age-dependent cognitive impairment and microglia accumulation within white matter tracts. *J Neuroinflammation*. 2018;15:241.
56. Braak H, Alafuzoff I, Arzberger T, Kretzschmar H, Del Tredici K. Staging of Alzheimer disease-associated neurofibrillary pathology using paraffin sections and immunocytochemistry. *Acta Neuropathol (Berl)*. 2006;112:389-404.
57. Kreisl WC, Lyoo CH, McGwier M, et al. In vivo radioligand binding to translocator protein correlates with severity of Alzheimer's disease. *Brain*. 2013;136:2228-2238.
58. Suridjan I, Pollock BG, Verhoeff NPLG, et al. In-vivo imaging of grey and white matter neuroinflammation in Alzheimer's disease: a positron emission tomography study with a novel radioligand, [18F]-FEPPA. *Mol Psychiatry*. 2015;20:1579-1587.
59. Birdsill AC, Kosciak RL, Jonaitis EM, et al. Regional white matter hyperintensities: aging, Alzheimer's disease risk, and cognitive function. *Neurobiol Aging*. 2014;35:769-776.
60. Balthazar MLF, Yasuda CL, Pereira FR, Pedro T, Damasceno BP, Cendes F. Differences in grey and white matter atrophy in amnesic mild cognitive impairment and mild Alzheimer's disease. *Eur J Neurol*. 2009;16:468-474.
61. Nowrangi MA, Lyketsos CG, Leoutsakos J-MS, et al. Longitudinal, region-specific course of diffusion tensor imaging measures in mild cognitive impairment and Alzheimer's disease. *Alzheimers Dement*. 2013;9:519-528.
62. Amlien IK, Fjell AM. Diffusion tensor imaging of white matter degeneration in Alzheimer's disease and mild cognitive impairment. *Neuroscience*. 2014;276:206-215.
63. Jack CR, Bernstein MA, Borowski BJ, et al. Update on the Magnetic Resonance Imaging core of the Alzheimer's Disease Neuroimaging Initiative. *Alzheimers Dement*. 2010;6:212-220.
64. Es ACGM van, Flier WM van der, Admiraal-Behloul F, et al. Lobar Distribution of Changes in Gray Matter and White Matter in Memory Clinic Patients: Detected Using Magnetization Transfer Imaging. *Am J Neuroradiol*. 2007;28:1938-1942.
65. Gouw AA, Seewann A, Vrenken H, et al. Heterogeneity of white matter hyperintensities in Alzheimer's disease: post-mortem quantitative MRI and neuropathology. *Brain J Neurol*. 2008;131:3286-3298.
66. Schetters STT, Gomez-Nicola D, Garcia-Vallejo JJ, Van Kooyk Y. Neuroinflammation: Microglia and T Cells Get Ready to Tango. *Front Immunol*. 2018;8.
67. Braestrup C, Squires RF. Specific benzodiazepine receptors in rat brain characterized by high-affinity (3H)diazepam binding. *Proc Natl Acad Sci U S A*. 1977;74:3805-3809.

68. Papadopoulos V, Baraldi M, Guilarte TR, et al. Translocator protein (18 kDa): new nomenclature for the peripheral-type benzodiazepine receptor based on its structure and molecular function. *Trends Pharmacol Sci.* 2006;27:402-409.
69. Selvaraj V, Stocco DM, Tu LN. Minireview: Translocator Protein (TSPO) and Steroidogenesis: A Reappraisal. *Mol Endocrinol.* 2015;29:490-501.
70. Bonsack F, Sukumari-Ramesh S. TSPO: An Evolutionarily Conserved Protein with Elusive Functions. *Int J Mol Sci.* 2018;19.
71. Itzhak Y, Baker L, Norenberg MD. Characterization of the peripheral-type benzodiazepine receptors in cultured astrocytes: Evidence for multiplicity. *Glia.* 1993;9:211-218.
72. Stephenson DT, Schober DA, Smalstig EB, Mincy RE, Gehlert DR, Clemens JA. Peripheral benzodiazepine receptors are colocalized with activated microglia following transient global forebrain ischemia in the rat. *J Neurosci.* 1995;15:5263-5274.
73. Beckers L, Ory D, Geric I, et al. Increased Expression of Translocator Protein (TSPO) Marks Pro-inflammatory Microglia but Does Not Predict Neurodegeneration. *Mol Imaging Biol.* 2018;20:94-102.
74. Chaney A, Bauer M, Bochicchio D, et al. Longitudinal investigation of neuroinflammation and metabolite profiles in the APP swe \times PS1 Δ e9 transgenic mouse model of Alzheimer's disease. *J Neurochem.* 2018;144:318-335.
75. Martín A, Boisgard R, Thézé B, et al. Evaluation of the PBR/TSPO Radioligand [18F]DPA-714 in a Rat Model of Focal Cerebral Ischemia. *J Cereb Blood Flow Metab.* 2010;30:230-241.
76. Tóth M, Little P, Arnberg F, et al. Acute neuroinflammation in a clinically relevant focal cortical ischemic stroke model in rat: longitudinal positron emission tomography and immunofluorescent tracking. *Brain Struct Funct.* 2016;221:1279-1290.
77. Defrise M, Kinahan PE, Michel CJ. Image Reconstruction Algorithms in PET. In: Bailey DL, Townsend DW, Valk PE, Maisey MN, eds. *Positron Emission Tomography: Basic Sciences.* London: Springer; 2005:63-91.
78. Hudson HM, Larkin RS. Accelerated image reconstruction using ordered subsets of projection data. *IEEE Trans Med Imaging.* 1994;13:601-609.
79. Levitan E, Herman GT. A Maximum a Posteriori Probability Expectation Maximization Algorithm for Image Reconstruction in Emission Tomography. *IEEE Trans Med Imaging.* 1987;6:185-192.
80. Gunn RN, Slifstein M, Searle GE, Price JC. Quantitative imaging of protein targets in the human brain with PET. *Phys Med Biol.* 2015;60:R363-411.

81. Logan J. Graphical analysis of PET data applied to reversible and irreversible tracers. *Nucl Med Biol.* 2000;27:661-670.
82. Fowler JS, Wang GJ, Logan J, et al. Selective reduction of radiotracer trapping by deuterium substitution: comparison of carbon-11-L-deprenyl and carbon-11-deprenyl-D2 for MAO B mapping. *J Nucl Med.* 1995;36:1255-1262.
83. Pike VW. Considerations in the Development of Reversibly Binding PET Radioligands for Brain Imaging. *Curr Med Chem.* 2016;23:1818-1869.
84. Wilson AA, Garcia A, Parkes J, et al. Radiosynthesis and initial evaluation of [18F]-FEPPA for PET imaging of peripheral benzodiazepine receptors. *Nucl Med Biol.* 2008;35:305-314.
85. Pike VW. PET Radiotracers: crossing the blood-brain barrier and surviving metabolism. *Trends Pharmacol Sci.* 2009;30:431-440.
86. Innis RB, Cunningham VJ, Delforge J, et al. Consensus nomenclature for in vivo imaging of reversibly binding radioligands. *J Cereb Blood Flow Metab.* 2007;27:1533-1539.
87. Logan J, Volkow ND, Fowler JS, et al. Effects of Blood Flow on [11C]Raclopride Binding in the Brain: Model Simulations and Kinetic Analysis of PET Data. *J Cereb Blood Flow Metab.* 1994;14:995-1010.
88. Sander CY, Mandeville JB, Wey H-Y, Catana C, Hooker JM, Rosen BR. Effects of flow changes on radiotracer binding: Simultaneous measurement of neuroreceptor binding and cerebral blood flow modulation. *J Cereb Blood Flow Metab.* 2019;39:131-146.
89. Mabrouk R, Strafella AP, Knezevic D, et al. Feasibility study of TSPO quantification with [18F]FEPPA using population-based input function. *PLoS ONE.* 2017;12.
90. Zanotti-Fregonara P, Chen K, Liow J-S, Fujita M, Innis RB. Image-Derived Input Function for Brain PET Studies: Many Challenges and Few Opportunities. *J Cereb Blood Flow Metab.* 2011;31:1986-1998.
91. Burger C, Buck A. Requirements and implementation of a flexible kinetic modeling tool. *J Nucl Med.* 1997;38:1818-1823.
92. Carson RE. Tracer Kinetic Modeling in PET. In: Bailey DL, Townsend DW, Valk PE, Maisey MN, eds. *Positron Emission Tomography: Basic Sciences.* London: Springer; 2005:127-159.
93. Poelwijk FJ, Tănase-Nicola S, Kiviet DJ, Tans SJ. Reciprocal sign epistasis is a necessary condition for multi-peaked fitness landscapes. *J Theor Biol.* 2011;272:141-144.
94. Lammertsma AA, Hume SP. Simplified reference tissue model for PET receptor studies. *NeuroImage.* 1996;4:153-158.

95. Rusjan PM, Wilson AA, Bloomfield PM, et al. Quantitation of Translocator Protein Binding in Human Brain with the Novel Radioligand [18F]-FEPPA and Positron Emission Tomography. *J Cereb Blood Flow Metab.* 2011;31:1807-1816.
96. Logan J, Fowler JS, Volkow ND, et al. Graphical Analysis of Reversible Radioligand Binding from Time—Activity Measurements Applied to [N-11C-Methyl]-(-)-Cocaine PET Studies in Human Subjects. *J Cereb Blood Flow Metab.* 1990;10:740-747.
97. Logan J. A review of graphical methods for tracer studies and strategies to reduce bias. *Nucl Med Biol.* 2003;30:833-844.
98. Bergström M, Awad R, Estrada S, et al. Autoradiography with positron emitting isotopes in positron emission tomography tracer discovery. *Mol Imaging Biol.* 2003;5:390-396.
99. Tong J, Williams B, Rusjan PM, et al. Concentration, distribution, and influence of aging on the 18 kDa translocator protein in human brain: Implications for brain imaging studies. *J Cereb Blood Flow Metab.* June 2019:271678X19858003.
100. Alam MdM, Lee J, Lee S-Y. Recent Progress in the Development of TSPO PET Ligands for Neuroinflammation Imaging in Neurological Diseases. *Nucl Med Mol Imaging.* 2017;51:283-296.
101. Kreisl WC, Fujita M, Fujimura Y, et al. Comparison of [11C]-(R)-PK 11195 and [11C]PBR28, Two Radioligands for Translocator Protein (18 kDa) in Human and Monkey: Implications for Positron Emission Tomographic Imaging of this Inflammation Biomarker. *NeuroImage.* 2010;49:2924-2932.
102. Mizrahi R, Rusjan PM, Kennedy J, et al. Translocator protein (18 kDa) polymorphism (rs6971) explains in-vivo brain binding affinity of the PET radioligand [18F]-FEPPA. *J Cereb Blood Flow Metab.* 2012;32:968-972.
103. Fujita M, Kobayashi M, Ikawa M, et al. Comparison of four 11C-labeled PET ligands to quantify translocator protein 18 kDa (TSPO) in human brain: (R)-PK11195, PBR28, DPA-713, and ER176—based on recent publications that measured specific-to-non-displaceable ratios. *EJNMMI Res.* 2017;7:84.
104. Zanotti-Fregonara P, Pascual B, Rostomily RC, et al. Anatomy of 18F-GE180, a failed radioligand for the TSPO protein. *Eur J Nucl Med Mol Imaging.* 2020.
105. Lyoo CH, Ikawa M, Liow J-S, et al. Cerebellum can serve as a pseudo-reference region in Alzheimer's disease to detect neuroinflammation measured with PET radioligand binding to translocator protein (TSPO). *J Nucl Med Off Publ Soc Nucl Med.* 2015;56:701-706.
106. Levit A, Regis AM, Garabon JR, et al. Behavioural inflexibility in a comorbid rat model of striatal ischemic injury and mutant hAPP overexpression. *Behav Brain Res.* 2017;333:267-275.

Chapter 2: TSPO PET Detects Acute Neuroinflammation but not Diffuse Chronically Activated MHCII Microglia in the Rat

The figure numbers were modified to fit in this thesis. Additional changes were made to this manuscript since being submitted for publication.

2.1 Introduction

Diffuse inflammation of brain white matter (WM) has been clinically implicated in the pathology of brain diseases including schizophrenia, traumatic brain injury, and Alzheimer's Disease [1–3]. In the continuum from mild cognitive impairment to Alzheimer's disease (AD), diffuse WM inflammation may explain why WM undergoes demyelination, tract disintegration, and atrophy while patients undergo cognitive decline [4–6]. To measure WM inflammation in living subjects, previous studies have used PET tracers that target the 18 kDa translocator protein (TSPO) [7,8]. TSPO is overexpressed in astrocytes and microglia during their activation, but the subtypes of activated microglia that express TSPO remains a subject of research.

Microglia that express major histocompatibility complex class II (MHCII) molecules, which are involved in antigen presentation, are considered to be proinflammatory [9]. MHCII molecules are correlated to cognitive dysfunction throughout AD and diffusely overexpressed in the WM microglia of patients with early-onset AD [1,10]. Previously, our group correlated diffuse MHCII activated microglia in WM with cognitive dysfunction in a prodromal transgenic rat model of AD that overexpresses human Swedish- and Indiana-mutated amyloid precursor protein (TgAPP21) to produce high levels of A β without depositing amyloid plaques [11–13]. We further demonstrated the importance of diffuse MHCII activated microglia by detecting them in WM remote to an ischemic subcortical stroke in an endothelin-1 (ET1) rat model that also exhibits

executive dysfunction [14,15]. Overall, these observations motivate the need to detect MHCII activated microglia *in vivo*.

In this study, we used the TgAPP21 and ET1-induced subcortical stroke rat models to investigate whether TSPO can detect diffuse MHCII activated microglia in WM. To quantify TSPO *in vivo*, we used a second-generation TSPO PET tracer ($[^{18}\text{F}]\text{FEPPA}$) and validated the cerebellum as a pseudoreference region [16]. TSPO-PET was validated using immunohistochemistry of TSPO, which was compared to the activated astrocyte marker GFAP and activated microglia markers iNOS and OX6 (MHCII) in ET1 rats.

2.2 Methods

2.2.1 Animals and Experimental Design

Animal ethics and procedures of this study are in compliance with the Canadian Council for Animal Care and Western University Animal Care Committee (Protocol 2014-016). Rats were housed under a 12h/12h light/dark cycle and received access to food and water *ad libitum*.

This study used male Fischer 344 rats aged 11-14 months. TgAPP21 (n = 11) and wild-type (n = 12) rats were randomly selected to investigate $[^{18}\text{F}]\text{FEPPA}$ uptake in WM of prodromal AD. Genotype was validated with PCR as previously described [13].

To study ischemic subcortical stroke, the same wild-type rats that received baseline *in vivo* imaging were randomly assigned to a stereotactic injection of 60 pmol endothelin-1 (ET1) dissolved in 3 μL sterile saline (n = 5) or sterile saline alone for control (n = 6) in the right dorsal striatum as previously described [17]. Rats were imaged *in vivo* post-stroke at day 7 and day 28, at which point they were euthanized for immunohistochemistry. A saline rat was omitted at day 7 because of a tail vein issue and 2 saline rats had to be replaced after baseline because they died.

An additional group of rats ($n = 5$ ET1, $n = 6$ saline) was euthanized at day 7 for acute immunohistochemistry.

2.2.2 In Vivo Imaging

Each *in vivo* imaging session consisted of a PET scan followed by MRI and CT. Before PET, anesthesia was administered at 2 L/min oxygen with 5% isoflurane for induction then maintained at 2% until after CT. Respiratory rate, heart rate, and body temperature were monitored and maintained throughout.

2.2.2.1 MRI

MRI was performed on a 3T MRI (Siemens Biograph mMR) with a dedicated quadrature rat brain coil (Cubresa, 44 mm inner diameter). 2D sagittal and axial T₂-weighted fast spin echo (FSE) images were acquired spanning the brain with an in-plane field-of-view (FOV) = (70 x 70) mm², matrix size = 320 x 320, in-plane resolution = (0.22 x 0.22) mm² and slice thickness = 1 mm. Other relevant parameters for the FSE sequence include: repetition time (TR) = 2930 ms (sagittal acquisition) and 3900 ms (axial acquisition), effective echo time = 97 ms, refocusing flip angle = 150°, echo train length = 11, bandwidth = 225 Hz/pixel, and averages = 4.

2.2.2.2 CT

For attenuation correction of the PET, full-body helical CT scans were acquired with a resolution of (0.20 x 0.20 x 1.25) mm³, tube current = 80 mA, tube voltage = 80 kVp, and rotation time = 1 s (GE Revolution CT). CT images were segmented using Hounsfield-unit thresholds into tissue and material types with known linear attenuation coefficients at 511 keV.

2.2.2.3 PET Acquisition and Processing

PET data was acquired dynamically over 90 minutes (Siemens Inveon). Thirty seconds after initiating the scan, 33.7 ± 5.6 MBq [^{18}F]FEPPA was injected through a tail vein catheter. On day 28, rat tail arteries were cannulated for blood sampling ($n = 4$). A blood volume of 50 μL was sampled into tubes with ethylenediaminetetraacetic acid at 2, 8, 16, 64, and 90 minutes post-injection. Blood was centrifuged to extract 15 μL of plasma, which was then loaded onto omniphilic cartridges (Oasis HLB, Waters). Fractions were eluted with 0%, 20%, and 40% acetonitrile in 1 mL of solution to elute successively more lipophilic metabolites [18]. Elutants, blood, and plasma were counted using a calibrated gamma detector.

Decay-corrected PET data from 70-90 minutes post-injection was used for standardized uptake value (SUV) analysis and dynamic frames of 1 x 27 s, 21 x 3 s, 12 x 10 s, 5 x 30 s, 4 x 60 s, and 16 x 300 s for pharmacokinetic modeling. Appendix B contains time-activity curve examples of the initial phase and full phase for the input function and critical regions as outlined in Fig. 2.1: infarct region, contralateral to the infarct region, ipsilateral corpus callosum, and contralateral corpus callosum. PET reconstruction consisted of 2 iterations of 3D ordered-subset expectation maximization followed by 18 iterations of fast maximum *a posteriori* (OSEM3D/FMAP) with a co-registered CT-based attenuation correction map.

2.2.2.4 PET Analysis

Co-registration, region of interest (ROI) segmentation, and data extraction were performed using 3D Slicer 4.10 [19]. Images were zero-interpolated to an isotropic 0.22 mm voxel size and linearly co-registered to define the ROI in each rat (Fig. 2.1). ROIs included the T₂w-hyperintense infarct region and contralateral to the infarct region for a positive control, periaqueductal gray, cerebellum, frontal cortex, WM forceps minor, corpus callosum proximal to the infarct, and corpus

callosum remote to the infarct. A 4 mm³ spherical ROI was placed in the centre of the cardiac left ventricular cavity to derive input functions. Input functions were corrected using biexponential and Hill function population fits of whole blood-to-plasma ratio and unmetabolized [¹⁸F]FEPPA-to-all metabolites ratio (MATLAB 2019a). Corrected input functions and time-activity curves were used with an assumed blood volume of 5% to solve for the Logan total distribution volume (DV – also known as V_T) and ratio (DVR) using custom MATLAB scripts. Standardized uptake value (SUV) was calculated based on weight and injected dose then used to calculate uptake ratios normalized to the cerebellum (UR).

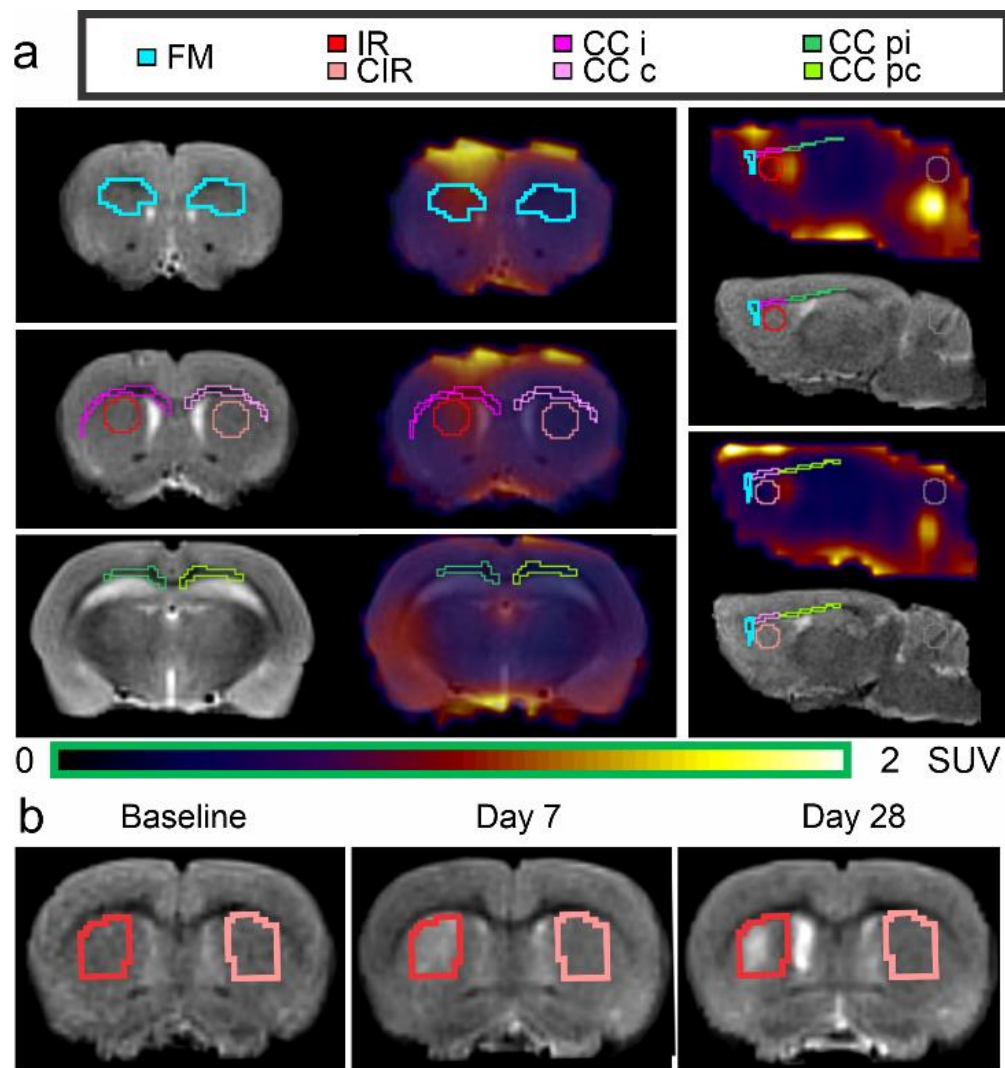


Fig 2.1 Analytical Methods. **a** Representative ROIs delineated on T₂w MRI and applied to fused [¹⁸F]FEPPA PET in a control rat at day 7. ROIs are proximal to the rat nose. **b** Infarct at baseline and post-stroke day 7 and 28 on T₂w MRI. c, contralateral; CC, corpus callosum; CIR, contralateral to the infarct region, FM: Forceps Minor; i, ipsilateral; IR, infarct region; p, posterior

2.2.3 Immunohistochemistry

All rats were euthanized with an intraperitoneal injection of pentobarbital (Euthanyl, Bimeda MTC Animal Health Inc) then underwent transcardiac perfusion using 10 mM phosphate-buffered saline (PBS) followed by 4% paraformaldehyde (PFA). Brains were extracted, fixed in 4% PFA for 24h, then stored at 4°C in 30% sucrose until they were cryosectioned into 30 μm thick sections (CryoStar NX50, Thermo Fisher Scientific). Sections were stored in cryoprotectant at -20 °C until

all tissue was available for 3,3'-Diaminobenzidine immunohistochemistry with avidin-biotin complex amplification (ABC Staining Kit, Thermo Fisher Scientific). Primary antibodies were anti-TSPO (1:1000, ab154878, abcam) for TSPO+ cells, anti-iNOS (1:1000, ab15323, abcam) for proinflammatory microglia, anti-OX6 (1:1000, #554926, BD Pharmingen) for MHCII, and anti-GFAP (1:2000, #G3893, Sigma-Aldrich) for activated astrocytes. We used anti-OX6 because it targets the rat MHCII gamma chain, which is necessary for the proper function of all MHCII molecules. GFAP is often used as a marker of activated astrocytes because they need it for reactive astrogliosis and scar formation.

The observer was blinded to experimental group during analysis. Images were acquired using a Nikon Eclipse Ni-E microscope and Nikon DS Qi2 colour camera on the NIS Elements Imaging software at a consistent lamp voltage and exposure for each antibody. TSPO cells were counted using four 20x sections at opposite borders of each defined *in vivo* region except the posterior corpus callosum, which used eight. Weak or diffuse staining was considered negative. GFAP, iNOS, and OX6 within-region % area coverage analysis used large images stitched from 10x magnification fields. Regions were manually defined using the polygon tool to replicate *in vivo* delineations of the proximal corpus callosum and forceps minor. The infarct and contralateral regions were also defined for iNOS. Images were binarized with a consistent threshold to get % area coverage within each region (ImageJ 1.52a) [12].

2.2.4 Statistical Analysis

All analyses of variance (ANOVA) were based on type III sum of squares (SPSS 26). To start, a two- or three-way ANOVA (depending on whether time was a variable) was conducted on PET (between ET1, within region and time) and immunohistochemistry (between ET1 and time, within region). Unless stated, higher-order interactions had to meet significance before analyzing simpler

effects with lower-order ANOVA and pooled variances if appropriate. Within-subject sphericities were accounted for using Greenhouse-Geisser corrections. Posthoc analyses for repeated timepoint effects were evaluated using Tukey's honestly significant differences (HSD) unless Shapiro-Wilk normality or Levene's variance assumptions were violated, in which case the Wilcoxon signed-rank or Mann-Whitney U test were used, depending on whether samples were paired. Correlation and graphing were performed on GraphPad Prism 7. All data is expressed as mean \pm standard deviation (SD). Significance was set at $\alpha = 0.05$.

2.3 Results

2.3.1 The Cerebellum is an Appropriate Pseudoreference Region for [¹⁸F]FEPPA PET

To determine an appropriate pseudoreference region for quantifying [¹⁸F]FEPPA uptake, [¹⁸F]FEPPA PET 70-90 min SUVs of the cerebellum and periaqueductal gray were compared (Figs. 2.2 and 2.3). The region contralateral to the infarct was also compared in the ET1 investigation. SUV was not significantly affected by genotype, ET1, or interaction between ET1 and timepoints ($P = \text{ns}$ for two-way and three-way ANOVA). Interestingly, region was a significant factor in both analyses of TgAPP21 vs. wild-type rats (A.U.: periaqueductal gray = 0.43 ± 0.14 ; cerebellum = 0.56 ± 0.18 ; $F(1,21) = 53.30$, $P < 0.0005$, two-way ANOVA) and ET1 vs. saline rats (A.U.: periaqueductal gray = 0.43 ± 0.12 ; region contralateral to the infarct = 0.49 ± 0.19 ; cerebellum = 0.60 ± 0.15 ; $F(2,12) = 27.47$, $P = 0.001$, three-way ANOVA). TSPO immunohistochemistry cell count of the day 28 infarct site also correlated better with the UR calculated using the cerebellum ($R^2 = 0.63$, $P = 0.0191$) instead of the region contralateral to the infarct ($R^2 = 0.47$, $P = \text{ns}$) or periaqueductal gray ($R^2 = 0.36$, $P = \text{ns}$) (Fig. 2.5). Accordingly, cerebellum-based [¹⁸F]FEPPA UR are reported hereafter.

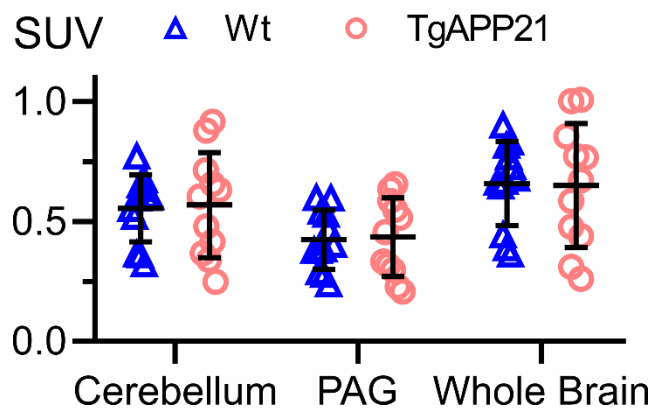


Fig 2.2 SUV was significantly different between the pseudoreference regions, cerebellum and PAG, in wild-type and TgAPP21 [$F(1,21)=53.30$, $P<.0005$, two-way ANOVA]. Whole brain SUV is also shown. CIR: contralateral to the infarct region. PAG: periaqueductal gray. Error = SD

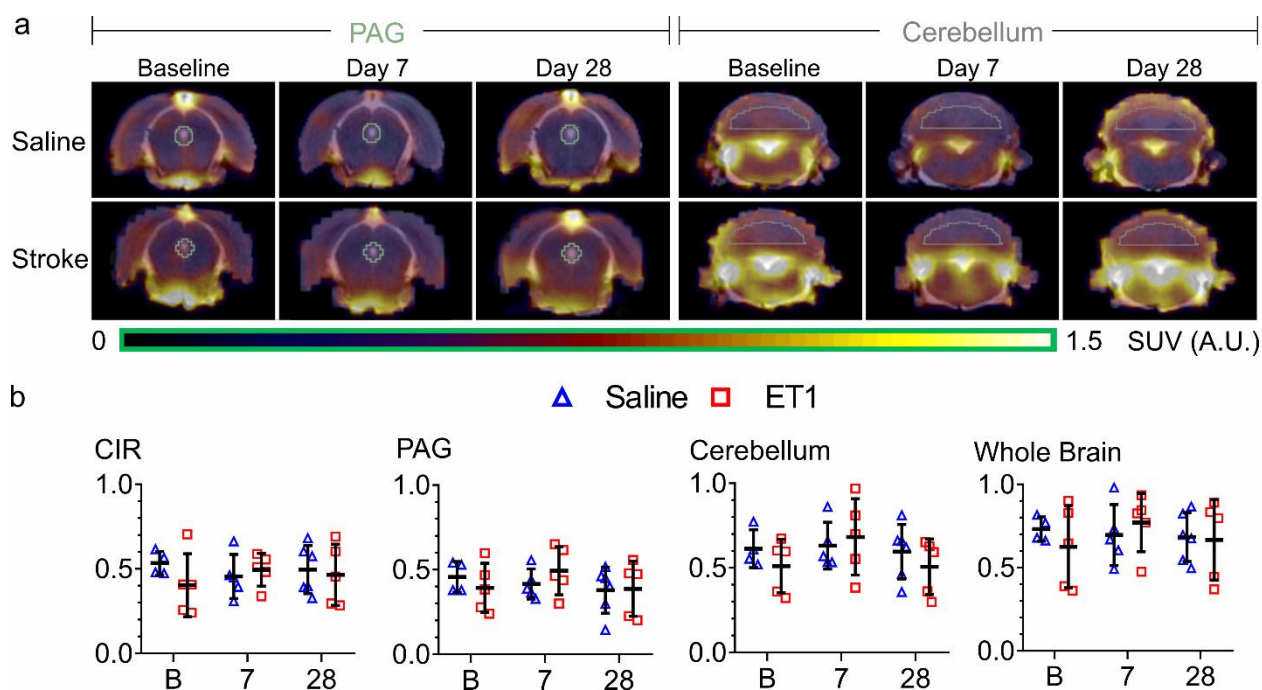


Fig 2.3 Wild-type saline and ET1 rat pseudoreference regions at baseline, day 7, and day 28 after an injection in the right dorsal striatum. (A) SUV maps overlaid on T₂-weighted MRI. (B) SUV showed a significant effect of region [$F(1,21)=53.30$, $P<.0005$, three-way ANOVA]. CIR, contralateral to the infarct region; PAG, periaqueductal gray. Error = SD

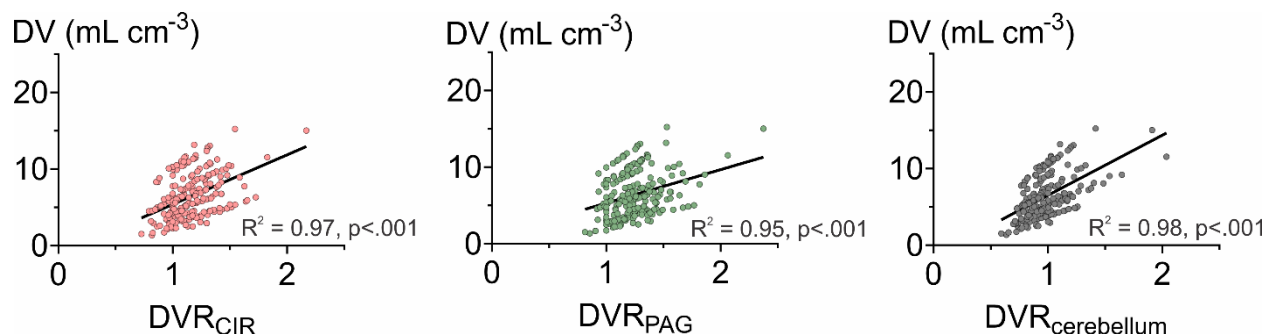


Fig 2.4 Correlations of distribution volume with distribution volume ratio to candidate pseudoreference regions. Each point represents one region in one Wt rat at the 28-day post-stroke timepoint. The coefficients of determination were derived within each rat, averaged, and are provided in the graph. CIR, contralateral to the infarct region; PAG, periaqueductal gray

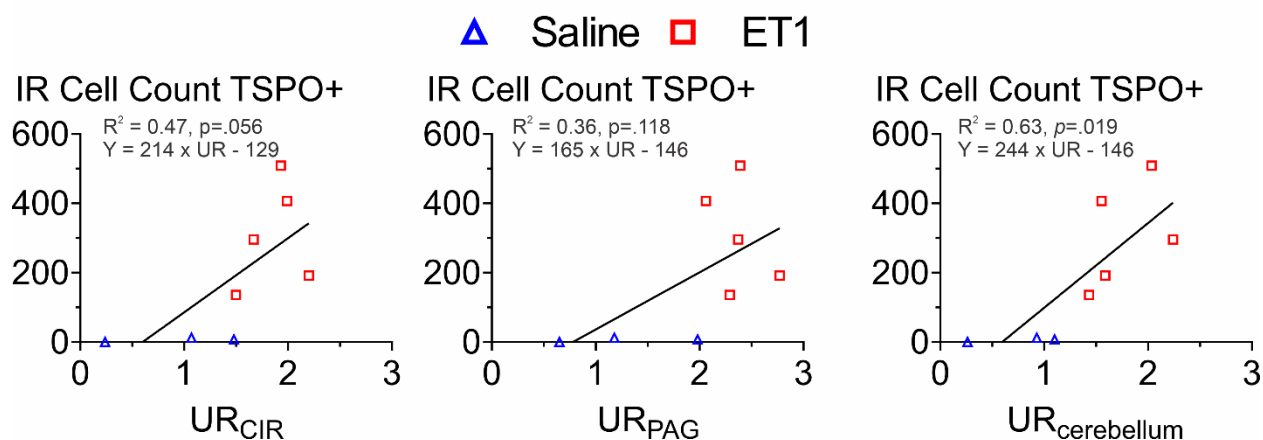


Fig 2.5 Correlations of infarct TSPO immunohistochemistry to uptake ratios calculated using candidate pseudoreference regions. Regression coefficients are provided in the graph. CIR, contralateral to the infarct region; PAG, periaqueductal gray; IR, Infarct region

2.3.2 [¹⁸F]FEPPA UR was not Elevated in WM of TgAPP21 Rats

UR in TgAPP21 and wild-type rats were analyzed to investigate [¹⁸F]FEPPA uptake in WM regions in which our group previously demonstrated MHCII microglial activation [12,13]. Genotype did not have a significant effect ($P = ns$, two-way ANOVA, Fig. 2.6). This suggested that [¹⁸F]FEPPA PET was not detecting the WM MHCII microglia that were previously reported in TgAPP21 rats.

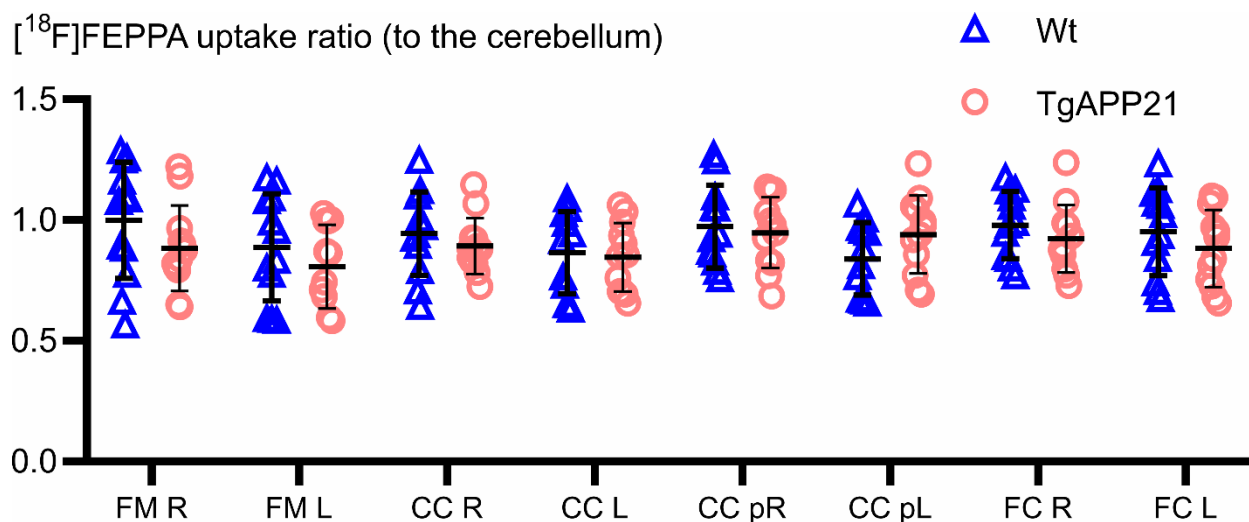


Fig 2.6 Transgenic amyloid precursor protein rats did not have an elevated [¹⁸F]FEPPA PET WM uptake ratio, to the cerebellum, relative to wild-type saline rats. Genotype effect was not significant ($P = \text{ns}$, two-way ANOVA). CC, corpus callosum; FC, frontal cortex; FM, Forceps Minor; p, posterior. Error = SD

2.3.3 [¹⁸F]FEPPA UR was not Elevated in Remote WM Following ET1-induced Stroke

UR at baseline, day 7, and day 28 after injection of ET1 or saline were analyzed to investigate [¹⁸F]FEPPA uptake in WM with the infarct as a positive control (Fig. 2.7). An interaction between region, timepoint, and ET1 suggested that UR was increased following ET1-induced stroke only in regions near the infarct [$F(20,120) = 3.66$, $P = 0.036$, three-way ANOVA]. In the infarct ROI of the ET1 group, UR significantly increased from baseline (0.94 ± 0.16) to day 7 (2.10 ± 0.78 ; $P = 0.043$, Wilcoxon signed-rank) and day 28 (1.77 ± 0.35 ; $P = 0.043$, Wilcoxon signed-rank). Similarly, proximal WM (ipsilateral corpus callosum) UR of the ET1 group significantly increased from baseline (0.94 ± 0.12) to day 7 (1.42 ± 0.34 ; $P < 0.005$, Tukey's HSD) and day 28 (1.38 ± 0.14 ; $P < 0.005$, Tukey's HSD). UR was not significantly affected in remote WM.

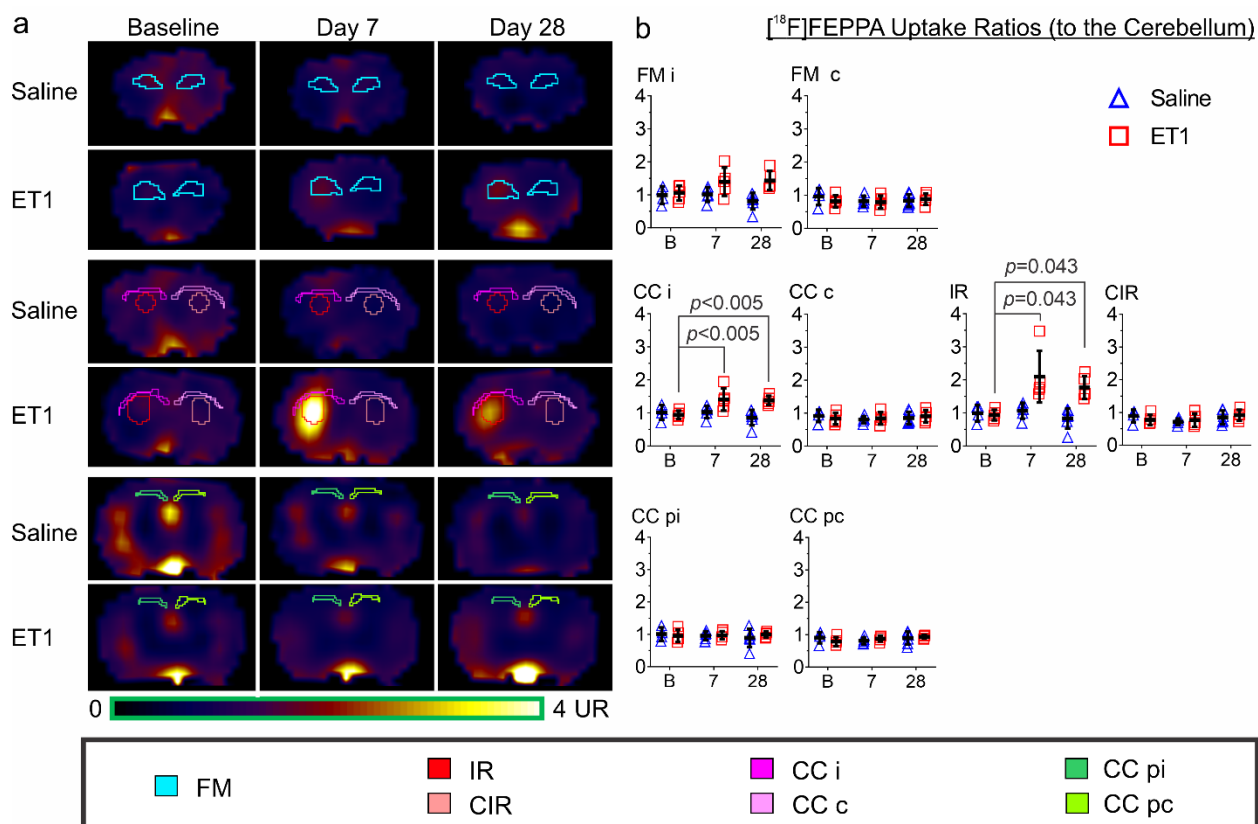


Fig 2.7 $[^{18}\text{F}]\text{FEPPA}$ UR was not elevated in remote WM following ET1-induced stroke. **a** Maps and **b** values of longitudinal $[^{18}\text{F}]\text{FEPPA}$ PET uptake ratio, relative to the cerebellum, revealed a significant region-ET1-timepoint interaction in saline and ET1 rats [$F(20,120) = 3.66$, $P = .036$, three-way ANOVA]. c, contralateral; CC, corpus callosum; CIR, contralateral to the infarct region; FM, Forceps Minor; i, ipsilateral; IR, infarct region; p, posterior. Error = SD

2.3.4 TSPO was not Expressed in Remote WM Following ET1-induced Stroke

TSPO immunohistochemistry-based cell counting was performed to confirm $[^{18}\text{F}]\text{FEPPA}$ PET findings in stroke. An interaction between region and ET1 suggested that TSPO immunohistochemistry concurred with $[^{18}\text{F}]\text{FEPPA}$ on the finding that ET1 increased TSPO only in regions near the infarct ($[F(9,117) = 27.04$, $P < 0.0005$], three-way ANOVA, Fig. 2.8). In the infarct, ET1 significantly increased TSPO cell count at day 7 (cells/mm²: saline = 48 ± 43 ; ET1 = 555 ± 181 ; $P = 0.014$, Mann Whitney U test) and day 28 (cells/mm²: saline = 6 ± 6 ; ET1 = 307 ± 153 ; $P = 0.025$, Mann Whitney U test). Proximal WM (ipsilateral corpus callosum) TSPO cell count agreed with $[^{18}\text{F}]\text{FEPPA}$ PET in regards to a day 7 elevation (113 ± 93 cells/mm²) but

disagreed by showing no day 28 elevation (5 ± 7 cells/mm²) (Fig. 2.9). Remote WM TSPO cell counts were low and unaffected by stroke (Figs 2.9 and 2.10). Recognizing that spillover of PET signal from the infarct into the ipsilateral corpus callosum might indicate an increased uptake in [¹⁸F]FEPPA PET when there is no TSPO overexpression, we used TSPO immunohistochemistry for further comparison of TSPO with GFAP, iNOS, and MHCII.

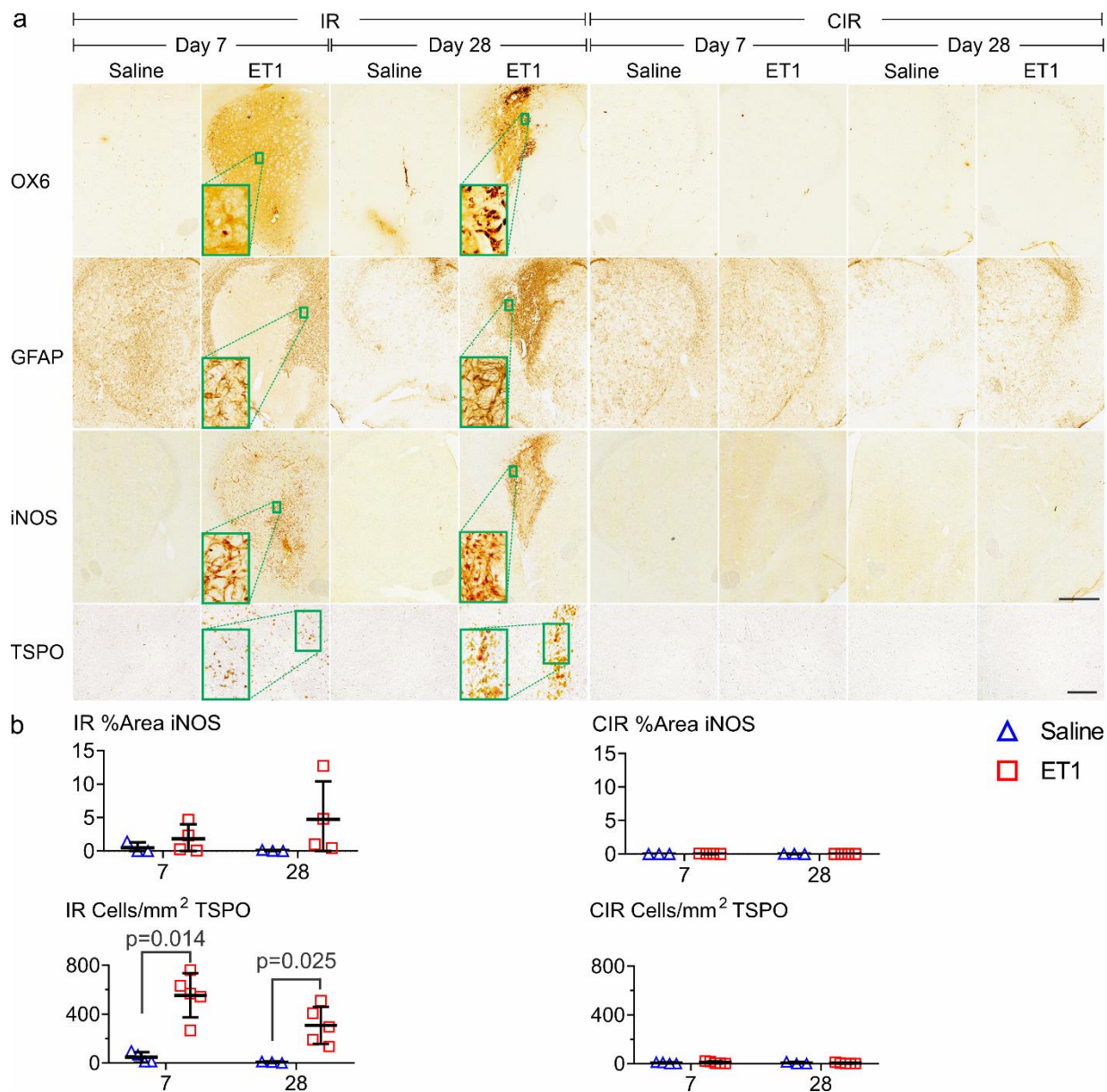


Fig 2.8 Immunohistochemistry showed that TSPO, but not iNOS, was elevated in the infarct site of ET1 rats at days 7 and 28 post-stroke. **a** Representative images of OX6 (MHCII), GFAP, iNOS, and TSPO in the infarct region (IR) and contralateral to the IR (CIR) post-stroke at day 7 and day 28 in saline and ET1 rats. **b** Quantification of cell count for TSPO and % area coverage for iNOS. Bar indicates 1 mm in large images and 100 μ m in TSPO. Error = SD

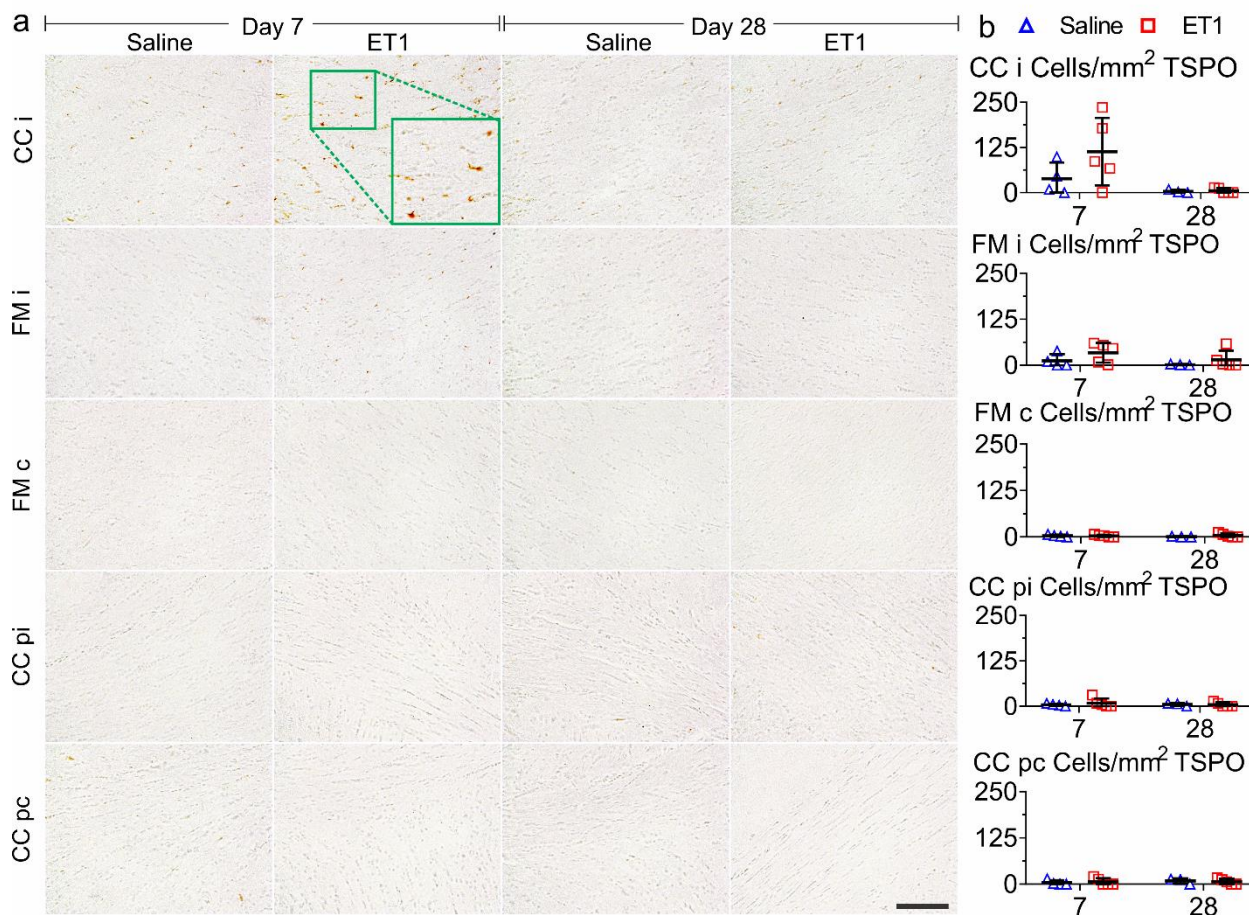


Fig 2.9 TSPO Immunohistochemistry of WM at day 7 and day 28 in saline and ET1 rats. (A) Representative images and (B) quantification of cell count for TSPO. FM, Forceps Minor; CC, corpus callosum; i, ipsilateral; c, contralateral; p, posterior. Bar indicates 100 μ m. Error = SD

2.3.5 GFAP and iNOS Expression was not Changed in WM Following ET1-induced Stroke

GFAP and iNOS immunohistochemistry were performed to further investigate changes in astrocytes and microglia as these markers are often compared with TSPO [20,21]. GFAP signal showed a day 7 border around the infarct and a day 28 scar in ET1 rats, but there were no significant effects in WM ($P = ns$, three-way ANOVA, Fig. 2.10). iNOS signal showed sensitivity to ET1 only in the infarct (% area: day 7 = 1.84 ± 2.16 ; day 28 = 4.74 ± 5.65 ; $P = ns$), without significance, and was not elevated in WM ($P = ns$, three-way ANOVA) (Figs. 2.8 and 2.10). Overall, GFAP and iNOS concurred with TSPO immunohistochemistry, with no significant changes in remote WM following ET1-induced stroke.

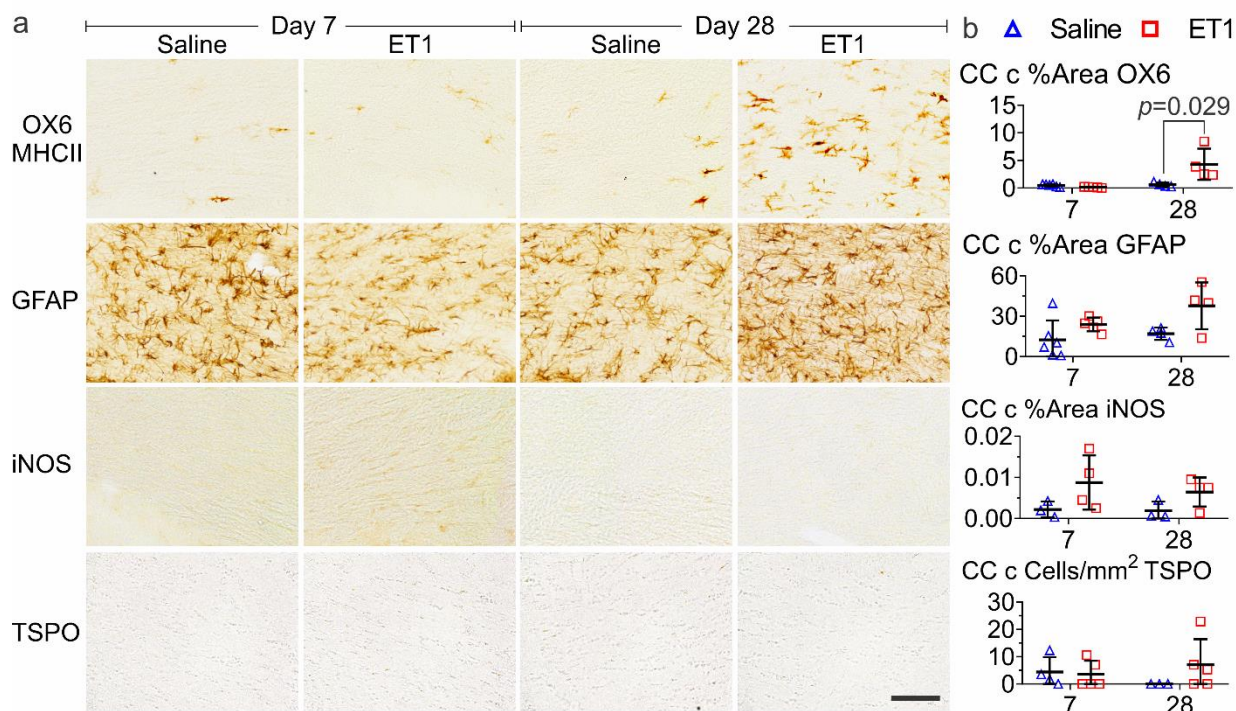


Fig 2.10 WM immunohistochemistry in the contralateral corpus callosum (CC c) showing that at 28 days post-stroke, ET1 rats only showed an elevation of OX6 (MHCII); not TSPO, iNOS, and GFAP. **a** Representative images and **b** quantification of cell count for TSPO and % area coverage for other markers. Bar indicates 100 μ m. Error = SD

2.3.6 MHCII-Positive Activated Microglia were Chronically Expressed in Remote WM Following ET1-induced Stroke

Immunohistochemistry of the MHCII rat antigen OX6 was used to confirm previous findings by our group of an ET1-induced increase of remote WM MHCII positive microglia activation (Fig. 2.10) [14,15]. WM OX6 signal was significantly affected by an interaction between timepoint and ET1 [$F(1,15) = 9.73$, $P = 0.007$, three-way ANOVA]. Although there were no significant interactions with region, we separately analyzed the contralateral corpus callosum at day 28 and found a significant effect of ET1 (% area saline = 0.62 ± 0.38 , ET1 = 4.30 ± 2.83 ; $P = 0.029$, Mann Whitney U test). This indicated that by day 28 post-stroke, MHCII was the only marker to show sensitivity to ET1 in WM.

2.4 Discussion

Literature about the non-specificity of TSPO to activated microglia is growing, but there are few reports showing that TSPO does not colocalize with all activated microglia or is not as sensitive as MHCII [22–24]. We found that [¹⁸F]FEPPA PET did not capture the expected increase of diffuse, chronically activated MHCII microglia in WM of TgAPP21 rats. Additionally, in an ET1-induced subcortical stroke model, MHCII microglia in remote WM were not detectable by [¹⁸F]FEPPA PET or TSPO immunohistochemistry.

The cerebellum was found to be an appropriate pseudoreference region. Other rodent AD studies have shown that the cerebellum is an acceptable pseudoreference region by demonstrating a lack of group effect on SUV [25]. When multiple pseudoreference regions are assessed in stroke, if the group effect is null for multiple regions, preference is sometimes given to the region with the lowest uptake [26]. Although SUV was lower in the periaqueductal gray and region contralateral to the infarct, we found that calculating UR using the cerebellum provided better correlations with TSPO immunohistochemistry and between DV and DVR. Using the cerebellum also ensured that our WM ROIs are sufficiently distant, thereby minimizing bias caused by partial volume effects. All of this suggests that the cerebellum is a practical pseudoreference for rodent TSPO PET studies of stroke and AD, but others should continue to investigate and validate their choice.

Although an increase in uptake of TSPO tracers in the infarct has been well documented, to our knowledge, rodent studies have only investigated cortical strokes as opposed to subcortical strokes [20,23,24,26]. In our study, we found that ET1-induced subcortical stroke infarcts have increased TSPO uptake at days 7 and 28 post-stroke. The proportion of TSPO signal from astrocytes cannot be deduced without multilabel immunofluorescence, but the formation of a

GFAP-positive astrocyte scar between days 7 and 28 suggests a change in astrocyte function that might explain why in other studies, TSPO expression tends to increase in astrocytes with time after a stroke [20,23,24]. Similarly, microglial functions seem to change as proinflammatory markers differ longitudinally; after day 7, some proinflammatory markers decrease while others, including iNOS, increase [27]. Our study similarly demonstrated that after day 7, iNOS increased while TSPO decreased, albeit insignificant partly due to high variability in rodent post-stroke iNOS expression [28]. For these reasons, TSPO PET may not provide unequivocal, longitudinal measurements for guiding subject-specific infarct-targeted anti-inflammatory therapy after stroke in rodent models.

Our findings suggest that TSPO does not capture diffuse WM inflammation in the TgAPP21 model or remote WM inflammation in the ET1-induced subcortical stroke model. WM TSPO studies in rodents have been restricted to mouse models of multiple sclerosis, which have focally elevated TSPO in active demyelinating lesions [29]. In the current study, prodromal AD TgAPP21 rats did not take up more [¹⁸F]FEPPA in WM, despite having previously demonstrated diffuse WM MHCII activated microglia [12]. Similarly, in ET1-induced subcortical stroke, WM TSPO expression was only increased in regions with focal inflammation and not in regions with diffuse inflammation. To our knowledge, TSPO overexpression in rodent WM without a nearby lesion has yet to be demonstrated.

TSPO mismatch with MHCII might be dependent on whether the pathology is associated with antigens that would induce the antigen-presenting function of MHCII in microglia. When antigens are not expected to induce pathology, TSPO is overexpressed without MHCII, as was shown in a rat model of alcohol-induced neurodegeneration [30]. Conversely, when lesions are present with antigenic alpha-synuclein, as in cases of human multiple system atrophy, post-mortem

tissue had a 6-fold increase in MHCII and 2-fold increase in TSPO relative to controls [22]. Our work in rats demonstrates that although TSPO detected neuroinflammation near the ET1-induced infarct, only MHCII was able to detect the WM microglial activation that occurred late post-stroke or in response to overexpression of pathogenic APP. Although this makes MHCII a desirable target for PET, its many genetic variants may pose a challenge.

This study has two main limitations. First, rat WM is small and susceptible to limits in PET resolution and sensitivity. To overcome this limitation, we used TSPO immunohistochemistry in rats injected with ET1 or saline to validate that TSPO is not sensitive to WM MHCII activated microglia. Second, this study used only males to minimize variables as females differ in their TSPO expression and neuroinflammatory response [31]. Whether males and females differ in their TSPO expression at an infarct or in WM should be further investigated.

In conclusion, we found that an ET1-induced subcortical stroke increases TSPO expression. More importantly, WM microglia only expressed TSPO near an ET1-induced lesion, thereby revealing that TSPO was insensitive to MHCII activated microglia in remote WM and in WM of prodromal AD rats without a lesion. An MHCII radiotracer would enable longitudinal imaging of chronically activated MHCII microglia in neurodegenerative diseases.

2.5 References

1. Raj D, Yin Z, Breur M, et al. Increased White Matter Inflammation in Aging- and Alzheimer's Disease Brain. *Front Mol Neurosci.* 2017;10:206.
2. Chiappelli J, Hong LE, Wijtenburg SA, et al. Alterations in frontal white matter neurochemistry and microstructure in schizophrenia: implications for neuroinflammation. *Transl Psychiatry.* 2015;5:e548.
3. Johnson VE, Stewart JE, Begbie FD, Trojanowski JQ, Smith DH, Stewart W. Inflammation and white matter degeneration persist for years after a single traumatic brain injury. *Brain.* 2013;136:28-42.
4. Kabani NJ, Sled JG, Chertkow H. Magnetization transfer ratio in mild cognitive impairment and dementia of Alzheimer's type. *NeuroImage.* 2002;15:604-610.
5. Nowrangi MA, Lyketsos CG, Leoutsakos J-MS, et al. Longitudinal, region-specific course of diffusion tensor imaging measures in mild cognitive impairment and Alzheimer's disease. *Alzheimers Dement.* 2013;9:519-528.
6. Balthazar MLF, Yasuda CL, Pereira FR, Pedro T, Damasceno BP, Cendes F. Differences in grey and white matter atrophy in amnesic mild cognitive impairment and mild Alzheimer's disease. *Eur J Neurol.* 2009;16:468-474.
7. Thiel A, Radlinska BA, Paquette C, et al. The temporal dynamics of poststroke neuroinflammation: a longitudinal diffusion tensor imaging-guided PET study with ¹¹C-PK11195 in acute subcortical stroke. *J Nucl Med.* 2010;51:1404-1412.

8. Suridjan I, Pollock BG, Verhoeff NPLG, et al. In-vivo imaging of grey and white matter neuroinflammation in Alzheimer's disease: a positron emission tomography study with a novel radioligand, [18F]-FEPPA. *Mol Psychiatry*. 2015;20:1579-1587.
9. Schettters STT, Gomez-Nicola D, Garcia-Vallejo JJ, Van Kooyk Y. Neuroinflammation: Microglia and T Cells Get Ready to Tango. *Front Immunol*. 2018;8:1905.
10. Parachikova A, Agadjanyan MG, Cribbs DH, et al. Inflammatory changes parallel the early stages of Alzheimer disease. *Neurobiol Aging*. 2007;28:1821-1833.
11. Agca C, Fritz JJ, Walker LC, et al. Development of transgenic rats producing human β -amyloid precursor protein as a model for Alzheimer's disease: Transgene and endogenous APP genes are regulated tissue-specifically. *BMC Neurosci*. 2008;9:28.
12. Levit A, Regis AM, Gibson A, et al. Impaired behavioural flexibility related to white matter microgliosis in the TgAPP21 rat model of Alzheimer disease. *Brain Behav Immun*. 2019;80:25-35.
13. Weishaupt N, Liu Q, Shin S, et al. APP21 transgenic rats develop age-dependent cognitive impairment and microglia accumulation within white matter tracts. *J Neuroinflammation*. 2018;15:241.
14. Weishaupt N, Riccio P, Dobbs T, Hachinski VC, Whitehead SN. Characterization of Behaviour and Remote Degeneration Following Thalamic Stroke in the Rat. *Int J Mol Sci*. 2015;16:13921-13936.

15. Weishaupt N, Zhang A, Deziel RA, Tasker RA, Whitehead SN. Prefrontal Ischemia in the Rat Leads to Secondary Damage and Inflammation in Remote Gray and White Matter Regions. *Front Neurosci.* 2016;10:81.
16. Wilson AA, Garcia A, Parkes J, et al. Radiosynthesis and initial evaluation of [18F]-FEPPA for PET imaging of peripheral benzodiazepine receptors. *Nucl Med Biol.* 2008;35:305-314.
17. Levit A, Regis AM, Garabon JR, et al. Behavioural inflexibility in a comorbid rat model of striatal ischemic injury and mutant hAPP overexpression. *Behav Brain Res.* 2017;333:267-275.
18. Katsifis A, Loc'h C, Henderson D, et al. A rapid solid-phase extraction method for measurement of non-metabolised peripheral benzodiazepine receptor ligands, [18F]PBR102 and [18F]PBR111, in rat and primate plasma. *Nucl Med Biol.* 2011;38:137-148.
19. Fedorov A, Beichel R, Kalpathy-Cramer J, et al. 3D Slicer as an image computing platform for the Quantitative Imaging Network. *Magn Reson Imaging.* 2012;30:1323-1341.
20. Martín A, Boisgard R, Thézé B, et al. Evaluation of the PBR/TSPO radioligand [(18)F]DPA-714 in a rat model of focal cerebral ischemia. *J Cereb Blood Flow Metab.* 2010;30:230-241.
21. Beckers L, Ory D, Geric I, et al. Increased Expression of Translocator Protein (TSPO) Marks Pro-inflammatory Microglia but Does Not Predict Neurodegeneration. *Mol Imaging Biol.* 2018;20:94-102.
22. Tóth M, Little P, Arnberg F, et al. Acute neuroinflammation in a clinically relevant focal cortical ischemic stroke model in rat: longitudinal positron emission tomography and immunofluorescent tracking. *Brain Struct Funct.* 2016;221:1279-1290.

23. Wang Y, Yue X, Kiesewetter DO, et al. [18F]DPA-714 PET Imaging of AMD3100 Treatment in a Mouse Model of Stroke. *Mol Pharm.* 2014;11:3463-3470.
24. Tong J, Williams B, Rusjan PM, et al. Concentration, distribution, and influence of aging on the 18 kDa translocator protein in human brain: Implications for brain imaging studies. *J Cereb Blood Flow Metab.* 2019;40:1061-1076.
25. López-Picón FR, Snellman A, Eskola O, et al. Neuroinflammation Appears Early on PET Imaging and Then Plateaus in a Mouse Model of Alzheimer Disease. *J Nucl Med.* 2018;59:509-515.
26. Chaney A, Cropper HC, Johnson EM, et al. 11C-DPA-713 versus 18F-GE-180: A preclinical comparison of TSPO-PET tracers to visualize acute and chronic neuroinflammation in a mouse model of ischemic stroke. *J Nucl Med.* 2018;60:122-128.
27. Hu Xiaoming, Li Peiying, Guo Yanling, et al. Microglia/Macrophage Polarization Dynamics Reveal Novel Mechanism of Injury Expansion After Focal Cerebral Ischemia. *Stroke.* 2012;43:3063-3070.
28. Collmann FM, Pijnenburg R, Hamzei-Taj S, et al. Individual in vivo Profiles of Microglia Polarization After Stroke, Represented by the Genes iNOS and Ym1. *Front Immunol.* 2019;10:1236.
29. Nack A, Brendel M, Nedelcu J, et al. Expression of Translocator Protein and [18F]-GE180 Ligand Uptake in Multiple Sclerosis Animal Models. *Cells.* 2019;8:94.

30. Marshall SA, McClain JA, Kelso ML, Hopkins DM, Pauly JR, Nixon K. Microglial activation is not equivalent to neuroinflammation in alcohol-induced neurodegeneration: the importance of microglia phenotype. *Neurobiol Dis.* 2013;54:239-251.

31. Tuisku J, Plavén-Sigraý P, Gaiser EC, et al. Effects of age, BMI and sex on the glial cell marker TSPO - a multicentre [11C]PBR28 HRRT PET study. *Eur J Nucl Med Mol Imaging.* 2019;46:2329-2338.

Chapter 3: Conclusion and Future Directions

3.1 Summary

In the introduction, the importance of WM in neuronal networks and the definition of inflammation were briefly discussed to provide background about WM inflammation, particularly WM microglial activation. The associations between WM disease and microglial activation in subcortical stroke and AD, along with their main pathologies, were also described. This was followed by a discussion of methods that can be used to measure WM microglial activation, with emphasis on TSPO-PET as the focus of this thesis. Importantly, the current thesis was motivated by the longitudinal ability of TSPO to mark microglial activation and our findings of cognitive impairment along with chronic microglial activation as detected by MHCII IHC in rat models of subcortical stroke and prodromal AD.

Our objectives and findings were:

1. **Objective:** To investigate WM microglial activation in a rat model of prodromal AD with TSPO-PET using the 2nd generation TSPO-PET radiotracer, [¹⁸F]FEPPA.

Finding: TSPO expression, as measured by [¹⁸F]FEPPA uptake ratio to cerebellum, was not elevated in the corpus callosum or forceps minor of a Fischer 344 rat mutated to overexpress a pathogenetic form of APP.

2. **Objective:** To investigate WM microglial activation longitudinally in a rat model of subcortical stroke with TSPO-PET.

Finding: TSPO expression, as measured by [¹⁸F]FEPPA uptake ratio to cerebellum, was not elevated in the corpus callosum or forceps minor of a Fischer 344 rat with subcortical stroke induced in the dorsal striatum by injection with the vasoconstrictor endothelin-1.

3. **Objective:** To investigate and validate WM TSPO expression in a rat model of subcortical stroke at 7-days and 28-days using IHC.

Finding: TSPO expression at 7-days and 28-days post-stroke, as measured by cell counting on IHC, was not elevated in the corpus callosum or forceps minor of a Fischer 344 rat with subcortical stroke induced in the dorsal striatum by injection with the vasoconstrictor endothelin-1.

4. **Objective:** To investigate WM microglial activation in a rat model of subcortical stroke using MHCII, iNOS, and GFAP IHC at 7-days and 28-days post-stroke.

Finding: The only elevated percent area measurement was that of MHCII at 28-days post-stroke in corpus callosum and forceps minor that were remote from the stroke site in a Fischer 344 rat with subcortical stroke induced in the dorsal striatum by injection with the vasoconstrictor endothelin-1.

5. **Objective:** To compare TSPO-PET and TSPO IHC to MHCII IHC in WM.

Finding: In a Fischer 344 rat model of subcortical stroke by endothelin-1, MHCII IHC showed chronic (28-days post-stroke) diffuse WM microglial activation in remote corpus callosum while TSPO-PET and TSPO IHC only showed WM microglial activation that was acute (7-days post-stroke) and proximal to a lesion.

The implications of these findings were discussed amongst others in chapter 2, but the main finding was that TSPO expression was not able to detect the chronic microglial activation in WM that is detectable by MHCII IHC. The implications of this finding are further discussed in the follow two sections.

3.2 TSPO in WM

Despite differences in TSPO expression between rats and humans, our findings may offer insight into studies investigating WM microglial activation with TSPO PET in human AD and subcortical stroke. In particular, our finding that TSPO was only overexpressed in the infarct and in WM near the infarct may help explain the disagreement between human AD studies. For example, a study by Kreisl et al. showed that WM TSPO uptake was similar between healthy controls, patients with mild cognitive impairment, and AD but did not report lesions [1]. Conversely, a study by Suridjan et al. showed higher TSPO uptake in AD patients with lesions [2]. It is therefore possible that the disagreement may be attributed to the presence of lesions. Furthermore, the current findings may help explain why after subcortical stroke, remote WM uptake of the TSPO radiotracer [¹¹C]PK11195 was elevated in patients with an infarct directly in the pyramidal tract while it was unaffected in patients with an infarct near a WM tract [3]. It is possible that the former induces a WM lesion by Wallerian degeneration with a severe inflammatory response and TSPO expression while the latter may not induce a lesion but, as we demonstrated in rats, it induces a delayed MHCII microglial activation with no TSPO expression. This cannot be confirmed as these patients were only tested for motor function and followed for 6 months after a stroke, however, the effects of subcortical stroke on cognitive impairment and dementia usually appear years later [4]. Overall, our findings suggest that the disagreement between human AD studies investigating WM microglial activation with TSPO-PET may be explained by the presence of lesions and that subcortical strokes that are not directly in a WM tract may not show WM microglial activation on [¹¹C]PK11195 PET because the damage is not severe enough to be associated with TSPO expression.

3.3 MHCII as a Marker of Microglial Activation

Although MHCII can be elevated in lesions, it can also be expressed without lesions. An example of a lesion where an elevated expression of MHCII has been often observed is senile plaques in people with AD [5]. On the other hand, non-lesion nonhuman primate studies where variation and risk factor factors were minimized demonstrated that the expression of MHCII increases with aging [6]. More recently, studies have shown that MHCII expression increases with aging specifically in the WM [7]. Overall, the expression of MHCII near senile plaques in people with AD, their increase with aging, and their increase with aging in WM suggest MHCII expression does not discriminate based on the presence of a lesion.

3.4 Limitations

3.4.1 Fischer 344 rat strain may have an overactive inflammatory response

An additional limitation of the study was the exclusive usage of the Fischer 344 rat strain, which may have an overactive chronic inflammatory response. Relative to the Sprague Dawley and Lewis rat strains, the Fischer 344 rats have a minimal ability to habituate; when Fischer 344 rats are repeatedly exposed to a stress, their stress response does not decrease in magnitude [8]. Additionally, a low habituation corresponds to an overactive chronic inflammatory response [9]. It is therefore possible that Fischer 344 rats have an overactive inflammatory response. Although other rat models may have a reduced MHCII microglial activation response to stroke or a TgAPP21 genotype, it is well known that MHCII microglial activation can be seen in human AD [5,7]. This suggests that human MHCII microglial activation may be modeled well by Fischer 344 rats.

3.4.2 Gray Matter in Subcortical Stroke and AD

Although there may be interest in the clinical importance of inflammation in the gray matter, we do not expect to find any significant inflammatory effects in the gray matter of our models, and

we therefore did not analyze all available gray matter regions using [^{18}F]FEPPA PET. To our knowledge, clinical studies of subcortical stroke have not reported microglial activation in gray matter outside the infarct site [3]. Similarly, clinical studies of AD only report brain microglial activation at sites of amyloid deposition, which are restricted to the neocortex and hippocampus [5,10–14]. For our models, we do not expect significant inflammatory effects in the gray matter because we observed, using immunohistochemistry, that (i) MHCII expression was much greater in the white matter regions than the gray matter regions and (ii) TSPO expression was not elevated in gray matter, except for at the injection site in some rats (data not shown). Specifically for the subcortical stroke model, this is in concordance with the clinical literature and our previous findings that a rat subcortical stroke does not lead to microglial overactivation in remote gray matter, although the stroke was thalamic instead of striatal [15]. As for the AD model, our current observations agree with our previous studies and make sense because the model is known to not deposit amyloid unless there is severe cerebral stress such as encephalitis [16–18]. Because we did not observe any gray matter inflammation previously in extensive studies or in the immunohistochemistry of this study, *in vivo* segmentation of gray matter was omitted from our methods and therefore analysis.

3.5 Future Directions

3.5.1 MHCII radiotracers

As stated in chapter 2, a future direction to pursue is the development of MHCII radiotracers, but this comes with challenges. To make accurate statements about MHCII molecules, a brief review of MHC nomenclature is necessary. The term MHC comes from George Davis Snell's discovery that the success of tissue transplants depends on genetically-determined histocompatibility [19]. This histocompatibility comes from a set of immune molecules that are genetically encoded by

what the peer-reviewed literature now refers to as the MHC, which in humans has 224 genes [20]. These MHC genes include those that encode for three distinct classes of immune molecules: MHCI for innate immunity, MHCII for adaptive immunity, and MHCIII for other molecules with a variety of functions (Fig. 3.1). While MHCIII gene products are only referred to as molecules, MHCI and MHCII gene products are interchangeably referred to as molecules and glycoproteins because the finished proteins have many complex carbohydrates groups [21]. MHC nomenclature is further complicated by how MHC, MHCI, MHCII, and MHCIII are only hypernyms. For example, MHC molecules in humans and rats are referred to as human leukocyte antigens (HLA) and RT1 (no full form) respectively [22] (Fig. 3.1). Overall, these facts suggest that care is required when referring to the MHC or its molecules.

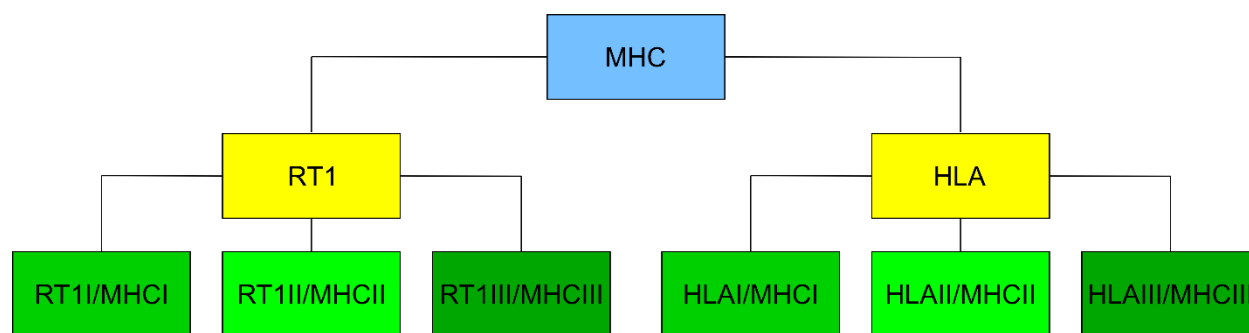


Fig 3.1 A visual summary of MHC nomenclature. MHC refers to the gene complex containing genes that encode the protein components of the three molecule classes: MHCI, MHCII, and MHCIII. Each of these classes has many molecules, which may be individually named according to the species (HLA in humans) for a variety of other reasons

With some genes in the MHC having over 500 alleles, the MHC is the most polymorphic region with phenotypic consequences in vertebrates [23]. In fact, the literature recognizes over 479 MHC-related traits [24]. This is largely thought to have evolved for the sake of maintaining a diverse set of immune responses in populations [23]. On the other hand, some of these traits include diseases that are associated with autoimmune pathology such as narcolepsy, rheumatoid arthritis,

type 1 diabetes mellitus, and AD [24,25]. In other words, although genetic mutations in the MHC may have led to a stronger immunity and population survival, many mutations led to disease.

Differences in MHCII genes and molecular expression are pathologically important. For example, some MHCII genes are associated with disease; over 90% of human autoimmune diseases are associated with the presence of these three MHCII allele combinations: HLA-DQ2/DR3, HLA-DQ6/DR2, and HLA-DQ8/DR4 [26]. Differences in molecular expression of MHCII have been observed in a variety of neurological pathologies, including schizophrenia, multiple sclerosis, multiple system atrophy, neuromyelitis optica, myasthenia gravis, Parkinson's disease, and AD [27–30]. Overall, MHCII molecules are a compelling target for the quantification of differences because of the association between MHCII expression and neurodegenerative diseases, and the occurrence of autoimmune diseases in people with specific MHCII gene combinations.

Although the polymorphism of MHCII poses a challenge, there may be representative targets without polymorphism. The polymorphism poses a challenge because differences in protein structure could make it unlikely for radioligands to bind every structure with a high enough affinity for PET imaging. Instead, there are representative targets without polymorphism including (i) the alpha chains in MHCII molecules, which are made up of an alpha chain and beta chain, (ii) the gamma chain, which transiently associates with many MHCII molecules during their folding and transport [20]. The alpha chain of HLA-DR is an exciting candidate because the alpha chain structure has been elucidated by high-resolution X-ray-crystallography (search on Uniprot, ID: P01903), there are several molecules known to interact with the alpha chain (also Uniprot), the sequence identity of humans has a 77% match with that of rats (Fig. 3.2), and HLA-DR indicates pathology according to post-mortem AD IHC studies [5,7]. Overall, MHCII polymorphism could

hinder radioligand binding, but there are alternative exciting targets with minimal or no polymorphism such as the HLA-DR alpha chain.

RT1 class II, locus Da precursor [Rattus norvegicus]

Sequence ID: [NP_001008847.1](#) Length: 255 Number of Matches: 1

[See 5 more title\(s\)](#) ▾

Range 1: 1 to 251 [GenPept](#) [Graphics](#)

▾ [Next Match](#) ▲ [Previous Match](#)

Score	Expect	Method	Identities	Positives	Gaps
406 bits(1043)	3e-141	Compositional matrix adjust.	193/251(77%)	215/251(85%)	0/251(0%)
Query 1	MAISGVVPLGFFIIAVLMSAQESWAIKEEHVIIQAEFYLNPDQSGEFMDFDGDGEIFHVD				60
Sbjct 1	MA G V+ FF +AVLMS Q+SVAI+EEH IIQAEFYL+PDQ+GEFMDFDGDGEIFHVD				60
Query 61	MAKETVWRLEEFGRFASFEAQGALANIAVDKANLEIMTKRSNYTPITNVPPEVTVLTNS				120
Sbjct 61	+ K ET+WRLEEF +FASFEAQGALANIAVDKANL+IM KRSN TP NV PEVTVL S IKKSETIWRLEEF				120
Query 121	PVELREPNVLICFIDKF+PPVNVNVTWLRNGKPVTTGVSETVFLPREDHLFRKFHYLPFLP				180
Sbjct 121	PV L EPN+LICFIDKF+PP VNVNVTWLRNG+PVT GVSETVFLPREDHLFRKFHYL FLP PVNLGEPNVLICFIDKF				180
Query 181	STEDVYDCRVEHWGLDEPLLKHWEFDAPSPLPETTENVVCALGLTVGLVGIIGTIFI				240
Sbjct 181	STED YDC V+HWGL+EPL KHWEF+ + LPET ENV+C LGL VGLVGI++G + IIK STEDYDCEVDHWGLEEPLRKHWEFEKTL				240
Query 241	GVRKSNAEAERR	251			
Sbjct 241	G+RK NA ERR				
	GLRKRNAVERR	251			

Fig 3.2 HLA-DR alpha chain alignment between humans and rats. The human HLA-DR alpha subunit has an identical 77% match with the laboratory rat species, *Rattus norvegicus*. The human HLA-DR alpha subunit, P01903, was set as a query with the algorithm set to search for the top 1000 matches on the NCBI blast website protein-protein (blast.ncbi.nlm.nih.gov). One of the matches, here shown as “Sbjct”, was the rat variant. The numbers flanking each row indicate the count of the amino acid. The middle row indicates the matching results: identical matches are echoed, non-matches are blank, and non-matches that are chemically similar are indicated with a positive sign positive (+)

3.5.2 Alzheimer’s Disease and Subcortical Stroke Comorbidity

Another direction to pursue is the comorbidity of subcortical stroke and AD because it increases the occurrence of dementia and, potentially, WM microglial activation. A heightened dementia occurrence has been attributed to subcortical stroke and AD comorbidity by the Nun study, which

demonstrated that a dementia diagnosis was not independently increased by the presence of brain infarcts, but the prevalence of dementia in those with AD pathology increased from 57% to 93% if they also had a subcortical infarct [31]. A recent hypothesis-generating paper has attributed this interaction to persistent post-stroke WM microglial activation as detected by [¹¹C]PK11195-PET [3]. Overall, the nun study findings of increased dementia when AD neuropathology is combined with subcortical stroke and the attribution of cognitive decline to WM microglial activation suggest that the comorbidity is a worthwhile direction to investigate.

Despite the increased occurrence of dementia when AD pathology is combined with subcortical stroke, very few large studies distinguish subcortical stroke from overall stroke [32,33]. These large studies will be necessary to gain a more representative understanding of their comorbidity.

3.5.3 Using PET to Guide WM Microglial Activation Therapy

TSPO-PET and, if developed, MHCII-PET, may be used to guide therapeutics that target microglial activation. PET is powerful in this regard because it allows microglial activation to be imaged longitudinally and in living people. By doing so, investigators can determine if therapeutics have an effect on microglial activation in WM of living people, the optimal dose, and whether the therapeutics have an optimal therapeutic window. For example, in AD, cholinesterase inhibitors such as Donepezil have been shown to be beneficial only when AD is mild or moderate [34]. In ischemic stroke, the field has recently been able to use *in vivo* imaging techniques, specifically diffusion-weighted MRI and perfusion CT, to extend the therapeutic window to 24 hours for which thrombectomy is beneficial [35]. By targeting WM microglial activation instead, it may be possible to slow the progression of or prevent chronic neurological and cognitive decline.

In particular, an MHCII radiotracer would be able to guide therapeutic approaches that target WM MHCII microglial activation for AD and chronic timepoints after subcortical stroke. It may also be used to guide therapeutics for some of the other neurodegenerative diseases that, as mentioned in a previous section, are associated with abnormal MHCII expression such as multiple sclerosis. Although TSPO-PET may not be able to guide therapeutics that target MHCII microglial activation, it may still be used to guide other types of microglial activation. For example, TSPO-PET was certainly able to detect the microglial and astrocyte activation that occurred in the infarct of the subcortical stroke.

3.6 Conclusion

The most significant finding of this study was that TSPO was unable to mark important pathology in the WM in rat models of subcortical stroke and AD. Because of this important finding, there is a strong case to be made for the development of MHCII radiotracers. One promising MHCII radiotracer target might be the MHCII HLA-DR alpha chain. If developed, it may be able to guide therapeutic approaches targeting WM inflammation. Furthermore, TSPO-PET may be used to guide therapeutic approaches that target the microglial and astrocyte activation that occurs in the infarct of the subcortical stroke. Additionally, TSPO-PET may also be used to image WM microglial activation that occurs after subcortical stroke that occurs directly in a WM target.

3.7 References

1. Kreisl WC, Lyoo CH, McGwier M, et al. In vivo radioligand binding to translocator protein correlates with severity of Alzheimer's disease. *Brain*. 2013;136:2228-2238.
2. Suridjan I, Pollock BG, Verhoeff NPLG, et al. In-vivo imaging of grey and white matter neuroinflammation in Alzheimer's disease: a positron emission tomography study with a novel radioligand, [18F]-FEPPA. *Mol Psychiatry*. 2015;20:1579-1587.
3. Thiel A, Radlinska BA, Paquette C, et al. The temporal dynamics of poststroke neuroinflammation: a longitudinal diffusion tensor imaging-guided PET study with 11C-PK11195 in acute subcortical stroke. *J Nucl Med*. 2010;51:1404-1412.
4. Norrving B. Long-term prognosis after lacunar infarction. *Lancet Neurol*. 2003;2:238-245.
5. McGeer PL, Itagaki S, Tago H, McGeer EG. Reactive microglia in patients with senile dementia of the Alzheimer type are positive for the histocompatibility glycoprotein HLA-DR. *Neurosci Lett*. 1987;79:195-200.
6. Sheffield LG, Berman NEJ. Microglial Expression of MHC Class II Increases in Normal Aging of Nonhuman Primates. *Neurobiol Aging*. 1998;19:47-55.
7. Raj D, Yin Z, Breur M, et al. Increased White Matter Inflammation in Aging- and Alzheimer's Disease Brain. *Front Mol Neurosci*. 2017;10:206.
8. Dhabhar FS, McEwen BS, Spencer RL. Adaptation to Prolonged or Repeated Stress – Comparison between Rat Strains Showing Intrinsic Differences in Reactivity to Acute Stress. *Neuroendocrinology*. 1997;65:360-368.
9. Thoma MV, Gianferante D, Hanlin L, Fiksdal A, Chen X, Rohleder N. Stronger hypothalamus-pituitary-adrenal axis habituation predicts lesser sensitization of inflammatory response to repeated acute stress exposures in healthy young adults. *Brain Behav Immun*. 2017;61:228-235.
10. Hyman BT, Trojanowski JQ. Editorial on Consensus Recommendations for the Postmortem Diagnosis of Alzheimer Disease from the National Institute on Aging and the Reagan Institute Working Group on Diagnostic Criteria for the Neuropathological Assessment of Alzheimer Disease. *J Neuropathol Exp Neurol*. 1997;56:1095-1097.
11. Hyman BT, Phelps CH, Beach TG, et al. National Institute on Aging–Alzheimer's Association guidelines for the neuropathologic assessment of Alzheimer's disease. *Alzheimers Dement*. 2012;8:1-13.
12. McGeer PL, McGeer EG. Inflammation, autotoxicity and Alzheimer disease. *Neurobiol Aging*. 2001;22:799-809.
13. McGeer PL, Rogers J, McGeer EG. Inflammation, anti-inflammatory agents and Alzheimer disease: The last 12 years. *J Alzheimers Dis*. 2006;9:271-276.

14. Liddel SA, Guttenplan KA, Clarke LE, et al. Neurotoxic reactive astrocytes are induced by activated microglia. *Nature*. 2017;541:481-487.
15. Weishaupt N, Riccio P, Dobbs T, Hachinski VC, Whitehead SN. Characterization of Behaviour and Remote Degeneration Following Thalamic Stroke in the Rat. *Int J Mol Sci*. 2015;16:13921-13936.
16. Levit A, Allman BL, Nagalingam R, Hachinski V, Whitehead S. Age-dependent white matter inflammation and cognitive impairment in the TgAPP21 rat model of Alzheimer disease. *Neurology*. 2018;91:242-242.
17. Weishaupt N, Liu Q, Shin S, et al. APP21 transgenic rats develop age-dependent cognitive impairment and microglia accumulation within white matter tracts. *J Neuroinflammation*. 2018;15:241.
18. Rosen RF, Fritz JJ, Dooyema J, et al. Exogenous seeding of cerebral β -amyloid deposition in β APP-transgenic rats. *J Neurochem*. 2012;120:660-666.
19. Hull P. Notes on DR Snell's observations concerning the H-2 Locus polymorphism. *Heredity*. 1970;25:461-465.
20. The MHC sequencing consortium. Complete sequence and gene map of a human major histocompatibility complex. *Nature*. 1999;401:921-923.
21. Ryan SO, Cobb BA. Roles for major histocompatibility complex glycosylation in immune function. *Semin Immunopathol*. 2012;34.
22. Günther E, Walter L. The major histocompatibility complex of the rat (*Rattus norvegicus*). *Immunogenetics*. 2001;53:520-542.
23. Piertney SB, Oliver MK. The evolutionary ecology of the major histocompatibility complex. *Heredity*. 2006;96:7-21.
24. Clark PM, Kunkel M, Monos DS. The dichotomy between disease phenotype databases and the implications for understanding complex diseases involving the major histocompatibility complex. *Int J Immunogenet*. 2015;42:413-422.
25. Lambert J-C, Ibrahim-Verbaas CA, Harold D, et al. Meta-analysis of 74,046 individuals identifies 11 new susceptibility loci for Alzheimer's disease. *Nat Genet*. 2013;45:1452-1458.
26. Mangalam AK, Rajagopalan G, Taneja V, David CS. HLA Class II Transgenic Mice Mimic Human Inflammatory Diseases. In: *Advances in Immunology*. Vol 97. Academic Press; 2008:65-147.
27. Tong J, Williams B, Rusjan PM, et al. Concentration, distribution, and influence of aging on the 18 kDa translocator protein in human brain: Implications for brain imaging studies. *J Cereb Blood Flow Metab*. June 2019:271678X19858003.

28. Durrenberger PF, Fernando FS, Kashefi SN, et al. Common mechanisms in neurodegeneration and neuroinflammation: a BrainNet Europe gene expression microarray study. *J Neural Transm.* 2015;122:1055-1068.
29. Fontana A, Gast H, Reith W, Recher M, Birchler T, Bassetti CL. Narcolepsy: autoimmunity, effector T cell activation due to infection, or T cell independent, major histocompatibility complex class II induced neuronal loss? *Brain J Neurol.* 2010;133:1300-1311.
30. Misra MK, Damotte V, Hollenbach JA. The immunogenetics of neurological disease. *Immunology.* 2018;153:399-414.
31. Snowdon DA, Greiner LH, Mortimer JA, Riley KP, Greiner PA, Markesbery WR. Brain infarction and the clinical expression of Alzheimer disease. The Nun Study. *JAMA.* 1997;277:813-817.
32. Honig LS, Tang M-X, Albert S, et al. Stroke and the Risk of Alzheimer Disease. *Arch Neurol.* 2003;60:1707-1712.
33. Toledo JB, Arnold SE, Raible K, et al. Contribution of cerebrovascular disease in autopsy confirmed neurodegenerative disease cases in the National Alzheimer's Coordinating Centre. *Brain.* 2013;136:2697-2706.
34. Birks JS, Harvey RJ. Donepezil for dementia due to Alzheimer's disease. *Cochrane Database Syst Rev.* 2018;18:CD001190.
35. Nogueira RG, Jadhav AP, Haussen DC, et al. Thrombectomy 6 to 24 Hours after Stroke with a Mismatch between Deficit and Infarct. *N Engl J Med.* 2018;378:11-21.

Appendices

Appendix A: Example Logan Solution

The Logan solution for a 2TCM may be derived using the equation defining the compartments in a tissue region as measured on pet (Eq1a), its integration (Eq1b), and the first-order kinetic equations for the exchange of radiotracer in the nondisplaceable compartment (Eq2) and bound compartment (Eq3).

$$\text{Eq 1a:} \quad C_T(t) = C_1(t) + C_2(t) + V_b C_B(t)$$

$$\text{Eq 1b:} \quad \int_0^t C_T(u) du = \int_0^t C_1(u) du + \int_0^t C_2(u) du + V_b \int_0^t C_B(u) du$$

$$\text{Eq 2:} \quad \frac{dC_1(t)}{dt} = K_1 C_p(t) - k_2 C_1(t) - k_3 C_1(t) + k_4 C_2(t)$$

$$\text{Eq 3:} \quad \frac{dC_2(t)}{dt} = k_3 C_1(t) - k_4 C_2(t)$$

Where for reversible tracer binding in a 2TCM:

$$V_T = \frac{K_1}{k_2} \left(1 + \frac{k_3}{k_4} \right)$$

C_T = Concentration of total radioactivity in the tissue

C_p = Concentration of free parent metabolite in the plasma

C_b = Concentration of total radioactivity in whole blood

C_1 = Concentration of parent metabolite in the nondisplaceable compartment

C_2 = Concentration of parent metabolite in the bound compartment

V_b = The ROI volume fraction of vascular tissue

K_1 = plasma-to-unbound-compartment transfer rate (delivery)

k_2 = unbound-compartment-to-plasma transfer rate (clearance)

k_3 = unbound-compartment-to-bound-compartment transfer rate (binding)

k_4 = bound-compartment-to-unbound-compartment transfer rate (unbinding)

The approach here is to express the integrals in equation 1b in terms of known variables. To do this, first derive simple expressions for the integrals.

For $\int_0^t C_1(u) du$, differentiate equation 1a, substitute in equations 2 and 3 and simplify, integrate, then rearrange:

$$\begin{aligned}\frac{dC_T(t)}{dt} &= \frac{dC_1(t)}{dt} + \frac{dC_2(t)}{dt} + V_b \frac{dC_B(t)}{dt} \\ \frac{dC_T(t)}{dt} &= K_1 C_p(t) - k_2 C_1(t) + V_b \frac{dC_B(t)}{dt} \\ C_T(t) &= K_1 \int_0^t C_p(u) du - k_2 \int_0^t C_1(u) du + V_b \int_0^t C_B(u) du \\ \int_0^t C_1(u) du &= \frac{1}{k_2} \left[K_1 \int_0^t C_p(u) du - C_T(t) + V_b \int_0^t C_B(u) du \right]\end{aligned}$$

For $\int_0^t C_2(u) du$, integrate equation 3 then rearrange:

$$\begin{aligned}C_2(t) &= \int_0^t k_3 C_1(u) du - \int_0^t k_4 C_2(u) du \\ \int_0^t C_2(u) du &= \frac{1}{k_4} \left[\int_0^t k_3 C_1(u) du - C_2(t) \right]\end{aligned}$$

Now the integrals may be substituted into equation 1b and expanded before resubstituting in

$\int_0^t C_1(u) du$ again:

$$\begin{aligned}
\int_0^t C_T(u) du &= \frac{1}{k_2} \left[K_1 \int_0^t C_p(u) du - C_T(t) + V_b \int_0^t C_B(u) du \right] + \frac{1}{k_4} \left[\int_0^t k_3 C_1(u) du - C_2(t) \right] \\
&\quad + V_b \int_0^t C_B(u) du \\
\int_0^t C_T(u) du &= \frac{K_1}{k_2} \int_0^t C_p(u) du - \frac{C_T(t)}{k_2} + \frac{1}{k_2} V_b \int_0^t C_B(u) du + \frac{k_3}{k_4} \int_0^t C_1(u) du - \frac{C_2(t)}{k_4} \\
&\quad + V_b \int_0^t C_B(u) du \\
\int_0^t C_T(u) du &= \frac{K_1}{k_2} \int_0^t C_p(u) du - \frac{C_T(t)}{k_2} + \frac{1}{k_2} V_b \int_0^t C_B(u) du + \frac{k_3}{k_4} \frac{1}{k_2} \left[K_1 \int_0^t C_p(u) du \right. \\
&\quad \left. - C_T(t) + V_b \int_0^t C_B(u) du \right] - \frac{C_2(t)}{k_4} + V_b \int_0^t C_B(u) du
\end{aligned}$$

This can then be expanded and rearranged into the linear equation:

$$\begin{aligned}
\int_0^t C_T(u) du &= \frac{K_1}{k_2} \left(1 + \frac{k_3}{k_4} \right) \int_0^t C_p(u) du - \frac{1}{k_2} \left(1 + \frac{k_3}{k_4} \right) C_T(t) \\
&\quad + V_b \left(1 + \frac{1}{k_2} + \frac{k_3}{k_4 k_2} \right) \int_0^t C_B(u) du - \left(\frac{1}{k_4} \right) C_2(t)
\end{aligned}$$

But since $C_T(t)$ is known, this equation may be made more stable by dividing both sides by $C_T(t)$:

$$\begin{aligned}
\frac{\int_0^t C_T(u) du}{C_T(t)} &= \frac{K_1}{k_2} \left(1 + \frac{k_3}{k_4} \right) \frac{\int_0^t C_p(u) du}{C_T(t)} - \frac{1}{k_2} \left(1 + \frac{k_3}{k_4} \right) + V_b \left(1 + \frac{1}{k_2} + \frac{k_3}{k_4 k_2} \right) \frac{\int_0^t C_B(u) du}{C_T(t)} \\
&\quad - \left(\frac{1}{k_4} \right) \frac{C_2(t)}{C_T(t)}
\end{aligned}$$

Appendix B: Time-activity curves

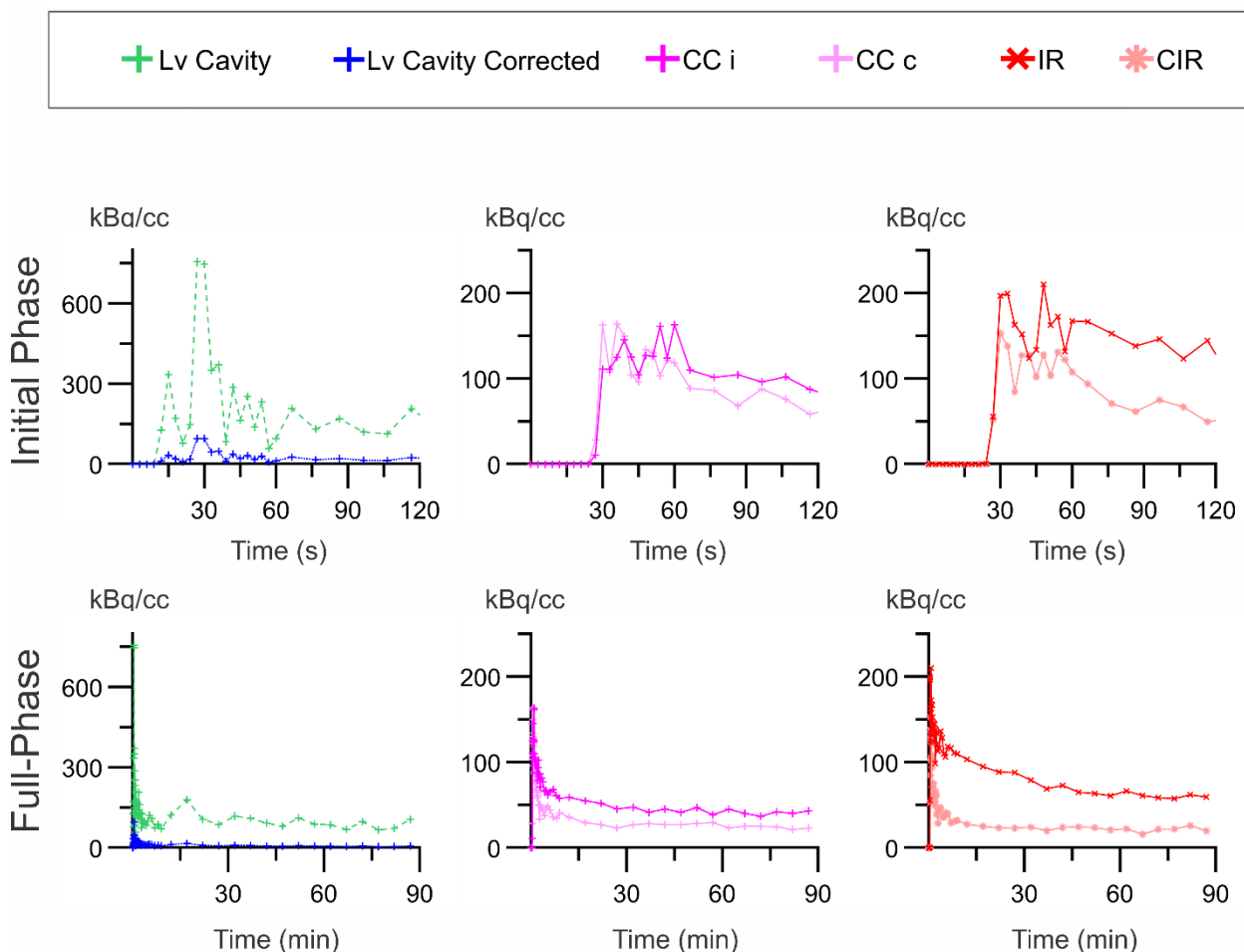


Figure A.1. Time-activity curves. Representative day-28 post-stroke ET1 rat time-activity curves.

The top row shows the initial phase with its time = 0 s equating to 27 s of the dynamic scan. The bottom row shows the full dynamic scan. Time-activity curves of the input function from the cavity of the left ventricle were corrected for the fraction of parent radiotracer that was free in the plasma. c, contralateral; CC, corpus callosum; CIR, contralateral to the infarct region, FM: Forceps Minor; i, ipsilateral; IR, infarct region; Lv, left ventricle.

Appendix C: Animal Use Ethics Approval

From: eSirius3GWebServer
To: [REDACTED]
Shawn Whitehead; Animal Care Committee
Cc: [REDACTED]
mgrsmtgs@uwo.ca
Subject: eSirius3G Notification -- 2018-132 New Protocol Approved
Date: October-11-18 4:02:35 PM



AUP Number: 2018-132

PI Name: Whitehead, Shawn N

AUP Title: Role of vascular risk factors in cognitive decline

Approval Date: 10/01/2018

Official Notice of Animal Care Committee (ACC) Approval:

Your new Animal Use Protocol (AUP) 2018-132:1: entitled " Role of vascular risk factors in cognitive decline"

has been APPROVED by the Animal Care Committee of the University Council on Animal Care. This approval, although valid for up to four years, is subject to annual Protocol Renewal.

Prior to commencing animal work, please review your AUP with your research team to ensure full understanding by everyone listed within this AUP.

As per your declaration within this approved AUP, you are obligated to ensure that:

1) Animals used in this research project will be cared for in alignment with:

a) Western's Senate MAPPs 7.12, 7.10, and 7.15
http://www.uwo.ca/univsec/policies_procedures/research.html

b) University Council on Animal Care Policies and related Animal Care Committee procedures

http://uwo.ca/research/services/animalethics/animal_care_and_use_policies.htm

-

2) As per UCAC's Animal Use Protocols Policy,

- a) this AUP accurately represents intended animal use;
- b) external approvals associated with this AUP, including permits and scientific/departmental peer approvals, are complete and accurate;
- c) any divergence from this AUP will not be undertaken until the related Protocol Modification is approved by the ACC; and
- d) AUP form submissions - Annual Protocol Renewals and Full AUP Renewals - will be submitted and attended to within timeframes outlined by the ACC.

e)

http://uwo.ca/research/services/animalethics/animal_use_protocols.html

3) As per MAPP 7.10 all individuals listed within this AUP as having any hands-on animal contact will

- a) be made familiar with and have direct access to this AUP;
- b) complete all required CCAC mandatory training (training@uwo.ca); and
- c) be overseen by me to ensure appropriate care and use of animals.

4) As per MAPP 7.15,

- a) Practice will align with approved AUP elements;
- b) Unrestricted access to all animal areas will be given to ACVS Veterinarians and ACC Leaders;
- c) UCAC policies and related ACC procedures will be followed, including but not limited to:
 - i) Research Animal Procurement
 - ii) Animal Care and Use Records
 - iii) Sick Animal Response
 - iv) Continuing Care Visits

5) As per institutional OH&S policies, all individuals listed within this AUP who will be using or potentially exposed to hazardous materials will have completed in advance the appropriate institutional OH&S training, facility-level training, and reviewed related (M)SDS Sheets,

<http://www.uwo.ca/hr/learning/required/index.html>

Submitted by: Copeman, Laura
on behalf of the Animal Care Committee
University Council on Animal Care

AUC Chair Signature



Dr. Timothy Regnault,
Animal Care Committee Chair

The University of
Western Ontario
Animal Care Committee / University
Council on Animal Care
London, Ontario Canada
N6A 5C1
519-661-2111 x 88792 Fax
519-661-2028

auspc@uwo.ca

<http://www.uwo.ca/research/services/animalethics/index.html>

Appendix D: Curriculum Vitae

NASSIR AL-KHISHMAN

EDUCATION

University of Western Ontario 2014 Sep – Present

- Bachelor's Honours, Bachelor of Medical Sciences,
Medical Biophysics and Biochemistry 2014 Sep – 2018 Jun
- Master's Thesis, Master's of Science, Medical Biophysics 2018 Sep – Present

RESEARCH

PUBLICATIONS

Author: **Al-Khishman N.U.**, Qi Q., Roseborough A.D., Levit A., Allman B.L., Anazodo A.C., Fox M.S., Whitehead S.N. and Thiessen J.D. TSPO PET Detects Acute Neuroinflammation but not Diffuse Chronically Activated MHCII Microglia in the Rat. Submitted to *EJNMMI Research* on June 7, 2020.

PRESENTATIONS

Author: **Al-Khishman N.**, Roseborough A., Fox M.S., Qi Q., Levit A., Hachinski V., Whitehead S.N., and Thiessen J.D. Longitudinal MRI and TSPO-PET: Alzheimer's Disease Interacts with Subcortical Stroke through Inflammation. In: Proceedings of the 18th Annual IMNO Symposium, March 26th-27th, 2020. Virtual. Scientific Session 6: Neurology Imaging 1, Presentation 4

Author: **Al-Khishman N.**, Fox M.S., Qi Q., Roseborough A., Levit A., Hachinski V., Whitehead S.N., and Thiessen J.D. Longitudinal TSPO-PET and MRI of Subcortical Stroke: Regional Differences Between Transgenic Alzheimer's Disease and Wild Type Rats [abstract]. In:

Archives of the 2019 World Molecular Imaging Congress. September 4th-7th, 2019. Montreal, Quebec (QC). Scientific Session 12: Advances in Functional Neuroimaging and Neuroinflammation, Presentation 5

POSTERS

Author: **Al-Khishman N.**, Fox M.S., Qi Q., Roseborough A., Levit A., Hachinski V., Whitehead S.N., and Thiessen J.D. Post-stroke Changes in T2-weighted Signal, Inflammation, and Perfusion. In: Proceedings of the 17th Annual IMNO Symposium, March 28th-29th, 2019. London, Ontario (ON). Cardiac and Vascular Imaging Poster 11-12

Co-author: Fox M, Anazodo U, Wilk B, Qi Q, **Al-Khishman N**, VanGinkel M, Smailovic H, Thiessen J. (2018). Leveraging Preclinical Simultaneous PET/MRI for Translational Multiparametric and Molecular Imaging in the Human: the Lawson Imaging Experience. Imaging in 2020. Visualizing the Future of Health Care with MR Imaging. September 23rd-27th, 2018

Co-author: Fox M, Roseborough A, Qi Q, Smailovic H, **Al-Khishman N**, Dhanvantari S, Whitehead S, Thiessen J. Possible Colocalization of Remote Tissue Inflammation Using Autoradiography and Immunohistochemistry in a Model of Ischemic Stroke. World Molecular Imaging Congress. Visualizing Biology to Improve Medicine September 12th-15th, 2018

Co-author: Qi Q, Gillespie G, Lim H, Al-Khishman N, Ahmed H, Bartha R, Hoffman L, Lee T-Y, and Thiessen JD. Multimodal in vivo imaging of perfusion and glycolysis in the C6 rat model of glioma. London Health Research Day, London, March 28, 2017

Co-author: Qi Q, Gillespie G, Lim H, Al-Khishman N, Ahmed H, Bartha R, Hoffman L, Lee T-Y, and Thiessen JD. Multimodal in vivo imaging of perfusion and glycolysis in the C6 rat model of glioma. Imaging Network of Ontario, London, March 15-16, 2017

RESEARCH WORK EXPERIENCE**SUMMER RESEARCH STUDENT**

2016 May – Aug and 2018 May – Sep

Lawson Research Institute, London, Canada

AWARDS AND RECOGNITIONS**Alexander Graham Bell Canada****Graduate Scholarship-Master's (CGS M)**

2019 Sep – 2020 Sep

17,500 (Canadian dollars)

Natural Science and Engineering Research Council of Canada

Western University, London, Ontario

World Molecular Imaging Society Student Travel Stipend Award

2019 Sep

350 (American dollars)

Montreal, Quebec, Canada

Western Graduate Research Scholarship (WGRS) x 2

2018 Sep – 2020 Sep

4,500 x 2 (Canadian dollars)

Western University, London, Ontario

International Learning Award

2016 Feb

1,000 (Canadian dollar)

Western University, London, Ontario

Dean's Honor List x 4

2015 Jul – 2018 Jul

Western University, London, Ontario

The Western Scholarship of Excellence

2014 Sep – 2015 Jun

2,000 (Canadian dollar)

Western University, London, Ontario

Western Scholar x 4

2014 Sep – 2018 Jun

Western University, London, Ontario